

Radio Continuum and Recombination Line Study of UC HII Regions with Extended Envelopes

Kee-Tae Kim

Department of Astronomy, Seoul National University, Seoul 151-742, Korea;
kimkt@astro.snu.ac.kr

and

Bon-Chul Koo

Astronomy Program, SEES, Seoul National University, Seoul 151-742, Korea;
koo@astrohi.snu.ac.kr

ABSTRACT

We have carried out 21 cm radio continuum observations of 16 UC HII regions using the VLA (D-array) in a search for associated extended emission. We have also observed H76 α recombination line towards all the sources and He76 α line at the positions with strong H76 α line emission. The UC HII regions have simple morphologies and large ($\gtrsim 10$) ratios of single-dish to VLA fluxes. We detected extended emission towards all the sources. The extended emission consists of one to several compact ($\sim 1'$ or 0.5–5 pc) components and a diffuse extended ($2'–12'$ or 4–19 pc) envelope. All the UC HII regions but two are located in the compact components, where the UC HII regions always correspond to their peaks. The compact components with UC HII regions are usually smaller and denser than those without UC HII regions. For individual sources, we derive the spectral types (O7–O4) of the ionizing stars and the fractions of UV photons absorbed by dust within the nebulae, which are significantly different from previous estimates based on the UC HII regions alone.

Our recombination line observations show that the ultracompact, compact, and extended components have approximately the same velocity in the individual sources with one exception (G25.72+0.05), implying that they are physically associated. The compact components in each object appear to be ionized by separate sources, while the UC HII regions and their associated compact components are likely to be ionized by the same sources on the basis of the morphological relations mentioned above. This suggests that almost all of the observed UC HII regions are not ‘real’ UC HII regions and that their actual ages are much greater than their dynamical age ($\lesssim 10^4$ yr). We find that most of simple UC HII regions previously known have large ratios of single-dish to VLA fluxes, similar to our sources. Therefore, the ‘age problem’ of UC HII regions does not seem to be as serious as earlier studies argued. We present a simple model in which the coexistence of the ultracompact, compact, and extended components for a long ($> 10^5$ yr) time is easily explained by combining the Champagne flow model

with the hierarchical structure of massive star-forming regions. The well-known relation between the density and diameter of HII regions, $n_e \propto D^{-1}$, is a natural consequence of the hierarchical structure according to our model. We discuss some individual sources.

Subject headings: HII regions— ISM: structure— radio continuum: ISM — radio lines: ISM

1. Introduction

Ultracompact (UC) HII regions are very small ($\lesssim 0.1$ pc) and dense ($\gtrsim 10^4$ cm $^{-3}$) ionized regions (Wood & Churchwell 1989a, hereafter WC89; Kurtz, Churchwell, & Wood 1994, hereafter KCW). They are bright radio and infrared sources and seem to be still embedded in the parental molecular clouds. Thus these objects have been thought to represent an early evolutionary stage of massive stars. One of the most interesting problems related to them is that too many UC HII regions are observed in the Galaxy, i.e., the “age problem”: The number of UC HII regions is greater by about an order of magnitude than expected from other indicators of massive star formation rate based on their dynamical age (WC89; Wood & Churchwell 1989b). Hence, it has been considered that HII regions should remain in the ultracompact phase for a much longer ($\gtrsim 10^5$ yr) period than their sound crossing time ($\lesssim 10^4$ yr) in a uniform medium. Several different models were proposed to resolve this problem: the infall model, photo-evaporating disk model, pressure-confined model, and stellar-wind supporting bow shock model (see Churchwell 2000 and references therein). These models present various mechanisms which constrain HII regions to remain longer in the ultracompact phase.

On the other hand, there is some observational evidence to suggest that UC HII regions are *not* as young as they appear. The ultracompactness of UC HII regions might arise because interferometric observations are insensitive to structures larger than a certain extent depending on the baseline range. Using the Very Large Array (VLA) D-array, which is sensitive to large ($\sim 15'$) structures, Koo et al. (1996) found that G5.48–0.24, known as an UC HII region, is actually a large HII region complex that contains structures of diverse length scales ranging from 0.04 to 40 pc: It has an ultracompact core, a compact core, an extended halo, and a diffuse large plateau. The presence of the extended envelope could be direct evidence supporting that the UC HII region is much older than 10^4 yr (see § 5 for more details). It also implies that there are much more ionizing photons than what would have been estimated from the ultracompact core alone. A few other groups have also noted the importance of extended emission around UC HII regions in understanding the nature of HII regions (Garay et al. 1993; Kurtz et al. 1999). For example, Kurtz et al. (1999) detected extended emission towards 12 out of 15 randomly selected sources from the KCW survey, and suggested on the basis of its morphology that the extended emission may be directly connected with UC HII regions in about half (8/15) of the sources. However, the physical relationship between UC HII regions and their extended envelopes is still poorly understood.

In this study, we undertook VLA radio continuum observations of 16 UC HII regions in search of associated extended emission and detected diffuse extended emission in all the sources. A preliminary version of these results was presented by Kim & Koo (1996). We also made H76 α and He76 α radio recombination line (RRL) observations in order to study the physical association between the UC HII regions and their extended envelopes. The observations are described in § 2 and the results are presented in § 3. We investigate the relationship between the parameters of the UC HII regions and their envelopes in § 4 and discuss the physical association between the two, the origin of extended envelopes, and their implication in resolving the age problem in § 5. Some individual

sources are discussed in § 6 and our main conclusions are summarized in § 7.

2. Observations

2.1. 21 cm Radio Continuum

We have carried out radio continuum observations of 16 UC HII regions with $\sim 40'' \times 20''$ resolution at 21 cm (Table 1). The observations were made during 1995 February using the VLA of the National Radio Astronomy Observatory¹ (NRAO) in the DnC hybrid configuration. So our observations are sensitive to structures smaller than $15'$. We have selected 16 UC HII regions from the WC89 catalog (Table 2). These UC HII regions are ones with simple morphology and large ($\gtrsim 10$) ratios of single-dish to VLA fluxes. Here simple morphology means that they each are not resolved into two or more clearly distinct components. This requirement is to avoid possible confusion by nearby UC HII regions in exploring the association between an UC HII region and extended emission. They consist of one shell-type, two spherical, three core-halo type, four cometary, and six irregular (or multiply peaked) UC HII regions. In order to improve the u - v coverage, each source was observed at several hour angles. The flux density was referred to 3C 286, which was assumed to have flux densities of 15.03 Jy (at 1.385 GHz) and 14.64 Jy (at 1.465 GHz). The data were edited, calibrated, imaged, and cleaned following the standard VLA procedures in the Astronomical Image Processing System (AIPS). Self-calibration was accomplished for several appropriate sources to reduce the rms noise level of their final images.

2.2. H76 α and He76 α Radio Recombination Lines

We observed H76 α RRLs, which have a rest frequency of 14,689.99 MHz, toward all of the objects in our sample. The observations were undertaken with the 140 foot (43 m) telescope of the NRAO in 1997 February and June. The telescope has an angular resolution (FWHM) of about $2'$ and a main beam efficiency of 0.58 at the observing frequency. In order to diminish the effects of standing waves between the telescope and receiver, we observed with focus alternately displaced $\pm \lambda/8$ from its peak value. Both circular polarizations were observed simultaneously using two 1024 channel autocorrelators with 40 MHz bandwidth each, and thus the velocity resolution was 1.59 km s^{-1} after Hanning smoothing. Each spectrum was obtained by integrating typically for 20 minutes using frequency switching. The system temperature varied in the range 40–60 K during the observing sessions depending on weather conditions and elevation of the source. We mapped G5.89–0.39 ($16' \times 10'$) and G5.97–1.17 ($18' \times 14'$) in full-beam spacing. For the other sources, we made observations at 1–13 positions including the peak positions in each envelope (see Figs.

¹ The National Radio Astronomy Observatory is operated by Associated Universities, Inc., under cooperative agreement with the National Science Foundation

1*a*–1*p*). He76 α (14,695.97 MHz) RRLs were also observed at a total of 18 positions in 6 sources (see Table 5). These positions are ones where strong H76 α line emission was detected.

3. Results

3.1. 21 cm Radio Continuum

We detected extended emission in all our sources. Figures 1*a*–1*p* show their images. The extended envelopes are from $2.'1 \times 1.'8$ to $14.'5 \times 10.'7$ in angular extent, and their morphologies range from a relatively simple structure with a single peak (e.g., G8.14+0.23, G23.71+0.17, and G23.96+0.15) to a fairly complicated structure with several compact components (e.g., G10.15–0.34, G10.30–0.15, and G29.96–0.02). All the UC HII regions except for G23.46–0.20 and G25.72+0.05 are located at the peak positions. Both of the latter are spherical UC HII regions lying near the edge of extended HII regions. If we adopt the distances given by WC89 (Table 2), the geometric mean diameters range from 0.56 pc to 5.68 pc for the compact components and from 3.8 pc to 18.7 pc for the extended envelopes. Based on their linear sizes (and physical parameters), the compact components would have been classified as compact or dense HII regions while the extended components would have been categorized as classical HII regions (Habing & Israel 1979). Table 3 presents the basic observed parameters of our sources. In the first column of this table, A–C represent the brightest three compact components in order of decreasing peak brightness. The first entry for each source refers to the extended component including UC HII region and compact component(s).

In the sources with two or more compact components, the UC HII regions tend to lie in the smallest and densest ones. This is shown in Figure 2, where we plot angular and linear sizes versus distance for the compact components. Most (11/14) of the compact components with UC HII regions are smaller than 2 pc, whereas all but two without UC HII regions are larger. The average diameter (1.6 pc) of the compact components with UC HII regions is about half of that of those without UC HII regions (3.5 pc). On the other hand, there seems to be no relationship between the morphologies of UC HII region and its extended envelope.

Assuming that the HII region is spherically symmetric, optically thin, homogeneous, dust-free, and ionization-bounded, we derived the electron number density n_e , emission measure EM , excitation parameter U , and mass M_{HII} of the ionized gas from the observed integrated flux densities (Schraml & Mezger 1969; Panagia & Walmsley 1978). We also estimated the Lyman continuum photon flux N'_c required to ionize each source using the formulae of Rubin (1968). Here we used the electron temperatures given by Downes et al. (1980) and Wink et al. (1982). Table 4 summarizes the results. The table also lists the spectral type of the ionizing star of each source (Panagia 1973). This assumes that a single zero-age main sequence (ZAMS) star is responsible for the ionization. The spectral types of the compact components with UC HII regions are approximately three subclasses earlier than those measured from UC HII regions alone in WC89, which are given in

parentheses. If a source is produced by a stellar cluster, rather than by a single star, then the most luminous star in the cluster would be about two subclasses later than the equivalent single-star spectral type (see, e.g., KCW). We determined the fraction of ultraviolet (UV) photons absorbed by dust within the ionized gas, $f_d=1-N'_c/N_c^*$, where N_c^* is the total rate of Lyman continuum photons of the ionizing star (Table 4). In this calculation, we adopted the value of N_c^* from WC89, which was derived primarily from the *IRAS* data under the assumption that a single star provides the entire infrared luminosity. We used the value of the associated (or the nearest) compact component for N'_c , considering the low ($\sim 4'$) resolution of *IRAS* observations. Our values of f_d might be overestimates because the sizes of the compact components are frequently smaller than the *IRAS* beamsize. In the majority (11/16) of our sources, nevertheless, the estimated fractions ($<60\%$) are significantly less than those ($\gtrsim 80\%$) determined by WC89 and KCW for most UC HII regions in their catalogs. This discrepancy may be mainly due to the contribution from extended emission around UC HII regions. Accordingly, the dust absorption of stellar UV radiation within the HII regions seems to be less important than suggested by previous studies.

3.2. H76 α and He76 α Radio Recombination Lines

We detected H76 α line emission in all the sources except G12.43–0.05, which was the weakest radio continuum source in our sample. Figure 3 shows a sample from our RRL spectra at G10.15–0.34 (+05 $^{\circ}$ 2, +00' 10''), where the strongest H76 α line emission was detected. We performed a least-squares fit of each spectrum to a single Gaussian profile. Table 5 gives the Gaussian parameters of the H76 α lines. In this table, columns (2)–(5) are the equatorial coordinates, the central velocity, the line intensity, and the line width (FWHM), respectively. The equatorial coordinates are given as offsets with respect to the position of UC HII region. Errors quoted are statistical $\pm 1 \sigma$ errors in the fit only. The central velocities of our RRLs detected toward UC HII regions are in good agreement with those of previous single-dish observations (Downes et al. 1980; Wink et al. 1982; Lockman 1989). We can find no significant velocity difference between the spectrum observed toward each UC HII region and the average spectrum of its extended envelope with one exception (G25.72+0.05). This indicates that the two components are physically associated. In the case of G25.72+0.05, H76 α line emission was observed at 98 km s $^{-1}$ toward the UC HII region while it was detected at 54 km s $^{-1}$ in the nearby compact component, suggesting that they constitute a chance coincidence in the line of sight. In seven sources (G5.89–0.39, G5.97–1.17, G10.15–0.34, G10.30–0.15, G12.21–0.10, G23.46–0.20, and G29.96–0.02), on the other hand, the ionized gas in some part of the envelope is blue- or redshifted by 3–10 km s $^{-1}$ with respect to the compact component associated with an UC HII region. For instance, the eastern part of G10.15–0.34 is blueshifted from its central region by ~ 10 km s $^{-1}$ (Fig. 4). We will discuss in detail the velocity structure of individual sources in § 6. The H76 α line width is usually larger in the compact components, especially in the ones with UC HII regions, than in the extended envelopes for the resolved sources (see § 6.1 and § 6.2). This trend probably occurs because turbulent motions, including large-scale expansion or contraction motions, are larger in the compact components than in the

extended envelopes, as proposed by Garay & Rodríguez (1983).

He76 α line emission was detected at 10 out of the 18 observed positions (Table 6). The singly ionized helium abundance (by number) Y^+ was estimated at these positions from the ratio of the He76 α to H76 α line integrals. The derived values (0.063–0.080) for G10.30–0.15, G23.46–0.20, and G29.96–0.02 are comparable to the average value (0.074 \pm 0.003) in our Galaxy (Shaver et al. 1983), while the values (0.016–0.049) for G5.89–0.39, G5.97–1.17, and G10.15–0.34 are significantly lower. The low value of Y^+ implies that either the sizes of HeII regions are significantly smaller than those of HII regions or the He abundance Y is low at the observed positions. For G5.89–0.39 and G5.97–1.17, the observed low value is likely to be due to the low effective temperature of the ionizing stars (O7) (Mezger 1980). Additionally these two objects are at galactocentric distances of 6–7 kpc where the metal abundance is known to be significantly higher than in the solar neighborhood (Shaver et al. 1983). The high metallicity could make the sizes of HeII regions smaller. This is not true for G10.15–0.34, which has ionizing stars of spectral type O5 or earlier. Such stars emit hard enough photons to singly ionize helium in the entire HII region. This view is supported by the fact that normal values were observed for Y^+ in G10.30–0.15, G23.46–0.20, and G29.96–0.02, which have ionizing stars of O5 or O5.5. We can also exclude the possibility that Y is low in the region because the value (≥ 0.063) is approximately normal in G10.30–0.15, which is located in the same molecular cloud (see § 6.3). A possible explanation for the low Y^+ observed in G10.15–0.34 is that helium ionizing photons are preferentially absorbed by dust in the nebula as in Sgr B2 (e.g., Chaisson, Lichten, & Rodríguez 1978).

4. Relationship between the Parameters of UC HII Regions and Their Extended Envelopes

4.1. Velocity

What is the physical relationship between the ultracompact, compact, and extended components in each source? According to our RRL observations, the compact component(s) and extended envelope appear to be physically associated in the individual sources. On the other hand, our measurements of the H76 α line emission toward UC HII regions were likely to be dominated by their associated compact components, rather than that due to the UC HII regions themselves, since our beam size ($\sim 2'$) is much larger than the typical size ($\lesssim 10''$) of the UC HII regions. In order to investigate the physical relationship between UC HII regions and their associated compact components, therefore, we compare our H76 α line data with the RRL and molecular line data of UC HII regions taken from the literature (Table 7). In this comparison, we do not include G12.43–0.05, in which the H76 α line was not detected. G23.46–0.20 and G25.72+0.05 are also excluded because they have no associated compact components. Figure 5 exhibits the results. On the whole, the central velocities of the two components are in rough agreement and there is no systematic trend between the two parameters. For 5 UC HII regions, our results are compared with those of high-resolution

RRL observations (Andrews et al. 1985; Churchwell et al. 1990b; Afflerbach et al. 1996). The central velocity of the UC HII region is equal to that of its associated compact component within 2 km s^{-1} for G6.55–0.10, G12.21–0.10, and G29.96–0.02, and within 6 km s^{-1} for G5.89–0.39 and G23.96+0.15. For the other UC HII regions, our H76 α lines are compared with their associated NH₃ or CS (7–6) lines (Churchwell et al. 1990a; Cesaroni et al. 1992; Plume et al. 1992). These molecular lines trace the densest part of a cloud, and their velocities should be close to those of UC HII regions (e.g., Forster et al. 1990). We could not find any significant ($\gtrsim 6 \text{ km s}^{-1}$) difference between the two velocities except for G23.71+0.17, for which the difference is $\sim 10 \text{ km s}^{-1}$. This large velocity difference is probably due to a relative motion between the ionized and molecular gas. Table 7 also presents the average difference between the velocities of the ultracompact and compact components, $\langle v_{\text{LSR,UC}} - v_{\text{LSR,C}} \rangle$, for each line emission.

4.2. Ionizing Photons

Figure 6 displays $N'_{\text{c,UC}}/N'_{\text{c,C}}$ versus $N'_{\text{c,C}}/N'_{\text{c,E}}$ for 14 sources in which the UC HII region has an associated compact component. Here $N'_{\text{c,UC}}$, $N'_{\text{c,C}}$, and $N'_{\text{c,E}}$ are the Lyman continuum photon fluxes of the ultracompact, compact, and extended components, respectively. For $N'_{\text{c,UC}}$, we used the values estimated by WC89 from flux densities at 2 cm or 6 cm. The ratios of $N'_{\text{c,C}}/N'_{\text{c,E}}$ are greater than 65% for all the sources with a single peak except for G5.97–1.17, which has a ratio of about 30%. On the other hand, $N'_{\text{c,UC}}/N'_{\text{c,C}}$ is less than 35% for 12 of the 14 sources. Our values of $N'_{\text{c,UC}}/N'_{\text{c,C}}$ and $N'_{\text{c,C}}/N'_{\text{c,E}}$ may be, respectively, overestimated and underestimated and so should be taken as upper limits and lower limits, since UC HII regions are optically thin at 2 cm or 6 cm but optically thick at 21 cm. The extreme cases are G5.89–0.39 and G29.96–0.02, for which $N'_{\text{c,C}}$ is equal to or less than $N'_{\text{c,UC}}$.

5. Discussion

5.1. Physical Association of UC HII Regions and Their Extended Envelopes

The UC HII region, compact component(s), and extended envelope in each source have approximately the same radial velocity and thus the three components are likely to be physically associated in almost all of our sources. Are they ionized by the same source or by separate sources? Although they are physically associated, they can still be ionized by separate sources, e.g., by stars of different ages in associations. This is closely related to how massive stars form from molecular clouds and how they destroy the natal clouds. First, in order to examine whether the compact components in each source are excited by the same ionizing source or not, we estimated how much Lyman continuum photon flux the ionizing star in the strongest compact component can provide for nearby components in sources with two or more compact components. Here it was assumed that the strongest component is density-bounded and the star maintains the ionization of the entire HII

region (including all compact components and extended envelope). The flux supplied depends on the solid angle subtended by the compact component from the ionizing star. The derived fluxes are much less (0.3%–30%) than the required values in all the sources. In the case of G10.15–0.34, for example, the ionizing source in the eastern compact component can supply the western one with at most 15% of the required flux. *Hence, the compact components in each source appear to be ionized by separate sources.*

What about the compact components and their envelopes? As stated in § 4.2, the ratios of $N'_{c,C}/N'_{c,E}$ are greater than 65% for all the sources with a single peak except for G5.97–1.17. The surface brightness decreases monotonically from the compact component peak to the envelope edge in these sources. *Therefore, it seems probable that the extended envelope is entirely or at least significantly ionized by the exciting star of the compact component.* In the case of sources with two or more compact components, the envelope of each compact component could have been produced by UV photons escaping from the compact component in a similar manner to the sources with a single peak. The individual envelopes might have merged to form a larger envelope at later times. However, we can not exclude absolutely the possibility that the large envelope may have been created by separate ionizing sources, such as massive stars in an earlier generation as in the sequential star formation model (Elmegreen & Lada 1977).

We can also ask whether the UC HII region and its associated compact component are excited by the same source or by separate sources. As noted in § 3.1, the UC HII regions correspond to the peaks of their associated compact components in all the sources and the compact components with UC HII regions are usually smaller and denser than those without UC HII regions. For three sources, i.e., G5.89–0.39, G6.55–0.10, and G29.96–0.02, we were able to confirm that the UC HII region is still located at the peak of radio continuum emission in available data obtained at higher resolution (Zijlstra et al. 1990; Andrews, Basart, & Lamb 1985; Fey et al. 1995). If they are ionized by independent sources, one would not expect these correlations. *Hence the UC HII region and its associated compact component are likely to be excited by the same ionizing source in our samples.* If this is true, the fractions of UV photons that escape from the UC HII regions, $f_{esc}=1-N'_{c,UC}/N'_{c,C}$, are estimated to be 65%–97% for our sources. These are probably underestimates (see § 4.2)

5.2. Is the Age Problem Solved?

The age problem of UC HII regions originates from the results of Wood & Churchwell (1989b), who found that UC HII regions have peculiar *IRAS* 60-12 μm and 25-12 μm colors, $\log(F_{60}/F_{12}) \geq 1.30$ and $\log(F_{25}/F_{12}) \geq 0.57$, and evaluated the total number of UC HII regions in the Galaxy to be 1650–3300 based on these color criteria. Since the *IRAS* sample is sensitivity-limited, most of them are likely to be embedded O stars. This estimate is about 10 times greater than the number derived from the known formation rate of O stars, e.g., 4×10^{-2} O stars yr^{-1} (see Garay & Lizano 1999), and the dynamical age ($\lesssim 10^4$ yr) of UC HII regions. However, almost all of the UC HII regions in our sample have extended (\gtrsim a few 1 pc) envelopes ionized by the same sources, which

implies that their actual ages are $\gtrsim 10^5$ yr (see next section). If most UC HII regions are associated with extended emission as in our sources, therefore, the age problem is expected to be resolved although we need to explain how structures with very different length scales can coexist in an HII region for a long time.

In order to address this issue, we calculated the ratios of single-dish (S_{SD}) to VLA fluxes (S_{VLA}) for 30 UC HII regions with simple morphology in the WC89 catalog. Here we used the 11 cm flux densities observed with the Effelsberg 100 m telescope (FWHM $\simeq 4'.3$) (Fürst et al. 1990). Most of the UC HII regions have large ratios (Fig. 7). For instance, about 70% have ratios >5 or $S_{VLA}/S_{SD} < 0.2$. The derived ratios are likely to be underestimated, since the UC HII regions are quite optically thick at 11 cm. However, this may have little effect on our result. One may suspect that the result is attributed to selection effects of the WC89 survey, because their original target list was created by selecting strong compact sources from previous single-dish surveys. Thus we also determined the flux ratios for 22 simple UC HII regions in the survey of KCW, which were chosen by the *IRAS* color criteria of Wood & Churchwell (1989b), and obtained a very similar result (Fig. 7). For comparison, we computed the ratios for the 15 sources of Kurtz et al. (1999), which consist of 8 simple and 7 complex UC HII regions. About 80% of the 12 sources with extended emission have ratios $\gtrsim 10$, while two of the 3 sources without extended emission have ratios < 5 . *Consequently, most sources known as UC HII regions are likely to be associated with extended emission, analogous to our sources.*

The *IRAS* color criteria of Wood & Churchwell (1989b) were established using the UC HII regions in the WC89 catalog. So the color criteria may select compact or extended HII regions as well as UC HII regions. This idea is consistent with the results of Codella, Felli, & Natale (1994) who found that more than half of 445 diffuse HII regions are related to *IRAS* point sources that satisfy the color criteria. We have investigated whether or not there is a systematic trend between the *IRAS* colors and S_{SD}/S_{VLA} . The *IRAS* colors may be expected to become bluer with increasing S_{SD}/S_{VLA} because the color criteria for the selection of *IRAS* point sources associated with diffuse HII regions are known to be bluer than those for UC HII regions (Hughes & MacLeod 1989). However, we could not find any apparent variation in the *IRAS* colors with S_{SD}/S_{VLA} , which implies that the *IRAS* colors are not very sensitive to the presence of extended emission.

5.3. Origin of Extended Envelopes

Our observations show that an UC HII region is usually surrounded by more extended emission, which appears to be excited by the same ionizing source. Various models were suggested to explain the longevity of UC HII regions, as mentioned in § 1, but none of them predicted the presence of extended emission around them. We consider the origin of the extended envelopes of UC HII regions in this section. Molecular clouds are well known to be hierarchically clumpy at all observable length scales. *Thus it is not surprising that HII regions, which form in molecular clouds, have substructures as in our sources.* Recent high-resolution studies of massive star-forming regions

have revealed “molecular clumps” and “hot cores” therein; the molecular clumps have diameters ~ 1 pc, masses $>10^3 M_{\odot}$, and densities $\sim 10^5 \text{ cm}^{-3}$, while the hot cores have diameters $\lesssim 0.1$ pc, masses of $(1-3)\times 10^2 M_{\odot}$, densities $>10^6 \text{ cm}^{-3}$, and temperatures $\gtrsim 100$ K (see Kurtz et al 2000 and references therein). The signposts of massive star formation, such as UC HII regions and maser sources, are commonly observed in the molecular clumps. The hot cores are closely associated with UC HII regions. They are believed to be the sites of massive star formation where UC HII regions have not yet developed (e.g., Cesaroni et al. 1994) or remnants of the gas from which the massive stars formed (e.g., Garay & Rodríguez 1990). The sizes of the hot cores and molecular clumps agree roughly with those of UC HII regions and their associated compact components in our sample, respectively.

We can first think of the possibility that the extended envelope could be formed very soon after the central star turns on, e.g., before the HII region starts to expand dynamically. It may depend on the density of interclump medium and volume filling factor of dense clumps. According to earlier studies on the internal structures of the molecular clumps in massive star-forming regions (Snell et al. 1984; Stutzki et al. 1988; Stutzki & Güsten 1990; Plume et al. 1997), the interclump medium density is generally $\gtrsim 10^4 \text{ cm}^{-3}$ and the volume filling factor varies between <0.1 and 0.5 and tends to increase with approaching the peak. Assuming that the spectral type of ionizing star is O6, the initial Strömgren radii of HII regions would be <0.15 pc, which are much less than the typical size of molecular clumps. To our knowledge, there is no previous detailed study on the substructures of the hot cores. However, both the interclump medium density and volume filling factor are expected to be greater in the hot cores, since they have much higher mean densities. Therefore, the extended envelope is likely to be formed by the dynamical expansion of ionized gas sphere. The existence of UC HII regions without extended envelopes, such as G23.46–0.20, G25.72+0.05 (§ 6.4), and G78.4+2.6 (Kurtz et al. 1999), also argues for this view.

We propose a simple model in which *the existence of the extended emission around UC HII regions can be explained by combining the Champagne flow model with the hierarchical structure of massive star-forming regions* (Tenorio-Tagle 1982 and references therein). Figure 8 is a schematic representation of our model. Here we consider the case where a massive star forms off-center within a hot core with $n_{\text{H}_2} \sim 10^7 \text{ cm}^{-3}$ and $M \sim 100 M_{\odot}$, which is placed in a molecular clump of $n_{\text{H}_2} \sim 10^5 \text{ cm}^{-3}$. The initial and final equilibrium Strömgren radii in this case are, respectively, about 0.0015 pc and 0.05 pc assuming $N'_c = 10^{49} \text{ s}^{-1}$ for the star (O6). A champagne flow would develop when an ionization front (of D-type) breaks out of the core. The timescale that the ionization front needs to reach the core’s edge depends on the depth of the exciting star inside the core. Assuming that the depth is 0.03 pc, the timescale will be $\sim 10^4$ yr from the expansion law for HII regions in a uniform medium (Spitzer 1968). If N'_c is significantly less than 10^{49} s^{-1} and/or n_{H_2} is greater than 10^7 cm^{-3} , the HII region can reach pressure equilibrium without breaking through the core’s boundary as in the pressure-confined model of UC HII regions (De Pree, Rodríguez, & Goss 1995; García-Segura & Franco 1996). The supersonic gas flow drives a strong isothermal shock moving away from the core and a rarefaction wave traveling toward the exciting star. The velocity of

the champagne flow, which is determined by the pressure contrast at the edge, could increase up to 30 km s^{-1} . According to Whitworth (1979) who estimated the efficiency with which O stars disperse their parental molecular clouds, the erosion timescale can be calculated from the following formula

$$t \approx 3 \times 10^5 \left(\frac{M}{10^2 M_\odot} \right)^{7/9} \left(\frac{N'_c}{10^{49} \text{ s}^{-1}} \right)^{-4/9} \left(\frac{n_{\text{H}_2}}{10^7 \text{ cm}^{-3}} \right)^{1/9} \quad (\text{yr}). \quad (1)$$

If this result is adopted, the lifetime of the hot core would be about 3×10^5 yr. Meanwhile, the HII region continues to be ultracompact within the hot core while it could grow up to a few 1 pc outside the core. Another champagne flow would develop when the ionization front crosses the edge of the molecular clump. Lyman continuum photons that escape from the clump ionize the surrounding region with a lower density, which forms a more extended HII region.

We could find the champagne flows in several sources § 3.2 based on the velocity gradient of H76 α line emission and/or the morphology of radio continuum image (see also § 6). This is compatible with expectation of our model. It is difficult to detect the champagne flows in all the sources because of the large line width and non-Gaussian profile of H76 α lines as well as various viewing angles. We may not expect to obtain direct evidence for the large velocity gradients on length scales of molecular clumps or smaller owing to the low resolution and coarse sampling of our RRL observations. However, the larger line width of RRLs in the compact components noted earlier is consistent with our model. In the light of the model presented here, among our sources G5.97–1.17 and G8.14+0.23 are good examples of HII regions observed at viewing angles of about 0° and 90° , respectively (see § 6.2 and § 6.6.2).

5.4. Density versus Size Relationship

For UC and compact HII regions, n_e was found to be on the average proportional to D^{-1} (Garay et al. 1993; Garay & Lizano 1999). Figure 9 compares electron density with diameter for the compact and extended components of our sources. There is a fairly good correlation between the two parameters. A least-squares fit yields $n_e = 630 D^{-0.93 \pm 0.05}$. Figure 9 also displays the relation between n_e and D for more compact HII regions in the catalogs of WC89, KCW, and Garay et al. (1993). We performed a least-squares fit to all the data points in the plot and obtained $n_e = 790 D^{-0.99 \pm 0.03}$.

If an HII region evolves with a constant flux of ionizing photons, n_e would be roughly proportional to $D^{-1.5}$. In view of this, the previous studies suggested two possible explanations for the shallower power law: either UC HII regions are excited by stars with lower luminosities than those exciting compact HII regions or a part of UC HII regions in the surveys of WC89 and KCW are externally ionized dense clumps within inhomogeneous HII regions. According to our model in § 5.3, however, the observed D – n_e relationship is not a manifestation of the evolutionary effect

but mainly of the variation in the ambient density; more compact HII regions are located in denser parts of molecular clouds. In this regard, it is natural to find a $D-n_e$ relationship which is similar to the $D-n_{\text{H}_2}$ relationship of molecular clouds, e.g., $n_{\text{H}_2} \propto D^{-1.1}$ (e.g., Larson 1981). There could be some evolutionary effects for larger HII regions, but Figure 9 shows that the effect does not make a significant contribution to the relationship for HII regions with $D \lesssim 20$ pc.

6. Discussion of Some Individual Sources

6.1. G5.89–0.39

G5.89–0.39, also known as W28 A2(1), is situated in W28 A2, which is $\sim 50'$ south of the W28 supernova remnant (SNR). This UC HII region was found to drive one of the most powerful ($\dot{P} \simeq 0.33 M_{\odot} \text{ km s}^{-1} \text{ yr}^{-1}$) molecular bipolar outflows (e.g., Accord, Walmsley, & Churchwell 1997) and thus has been extensively studied. In the VLA radio continuum maps with high ($< 1''$) resolution, G5.89–0.39 appears as a $\sim 5''$ shell (WC89) or a disk-like structure (Zijlstra et al. 1990). Previous estimates of the spectral type of the ionizing star range from O5 to O7.

Our radio continuum observations show that there are two compact components separated by $2'.5$ in this field: a large (1.1 pc) central one and a small (0.7 pc) western one (Fig. 1a). G5.89–0.39 is located in the western compact component. The two compact components are embedded in low-level emission extending over $14' \times 9'$ (or $10.9 \times 6.8 \text{ pc}^2$ at 2.6 kpc). The brightness distribution within the extended structure is fairly complicated. A bright ridge, originating from the central compact component, extends in the southwest direction. The surface brightness declines outward from the central region and then increases again at the edge of the extended structure. Figures 10a and 10b show the distributions of the H76 α line integral and equivalent line width ($\int T_{\text{L}} dv / T_{\text{L}}$) in this field, respectively. The line integral peak does not correspond to the central continuum peak but to the western peak with the UC HII region. The line width is largest (47 km s^{-1}) at the same position, as pointed out in § 3.2. This large line width is certainly attributed to the energetic outflow. The central velocity is slightly lower in the compact components than in the extended envelope.

6.2. G5.97–1.17

G5.97–1.17 lies in the well-observed HII region M8, the Lagoon nebula. M8 is placed in the Sagittarius arm of the Galaxy and contains an extremely young (about 1.5 Myr) open cluster, NGC 6530, in the eastern part (Sung, Chun, & Bessell 2000). The dense region ($\sim 10'$) of M8 in optical emission corresponds roughly to our radio HII region. The central part ($30'' \times 15''$ in NS \times EW) of the dense region is known as the Hourglass nebula. G5.97–1.17 and the Hourglass, respectively, lie $\sim 3''$ to the southeast and $\sim 15''$ east of the O7 V star Herschel 36, which is known to be a newly

formed star recently emerged from its dust cocoon (WC89; Woolf 1961). It was suggested that the dense region is ionized mainly by Herschel 36 while the more extended nebulosity is excited by the other O stars in NGC 6530, such as 9 Sgr (O4(f)) and HD 165052 (Oe) (Lada et al. 1976; Elliot et al. 1984). Based on their optical and radio observations showing that the ionized gas is blueshifted by about 7 km s^{-1} with respect to the underlying molecular cloud, Lada et al. (1976) proposed that the dense ionized region is on the near edge of the cloud, similar to the Orion Nebula. Stecklum et al. (1998) recently suggested that G5.97–1.17 is not a real UC HII region but a circumstellar disk surrounding a young star (later than B5), which is being photoevaporated by Herschel 36.

Our radio continuum observations reveal a single compact component surrounded by extended emission of $14.'5 \times 10.'7$ (or $8.0 \times 5.9 \text{ pc}^2$ at 1.9 kpc) (Fig. 1b). G5.97–1.17 and the Hourglass nebula are located in the compact component. Since the surface brightness declines monotonically from the UC HII region to the edge of the extended envelope, the ionizing source of our radio HII region is expected to be located in the compact component. Herschel 36 may be the best candidate. An interesting feature is the arclike structure emanating from the southeastern part of the envelope. Figures 11a and 11b show maps of the H76 α line integral and equivalent line width for this field, respectively. The distribution of the line integral is similar to that of continuum emission, but the line width is extraordinarily large at the bottom of the arclike structure. This large velocity dispersion is likely to be a consequence of the champagne flow, although the velocity difference between the arc and compact component is not large ($\sim 3 \text{ km s}^{-1}$). The central velocity appears to be larger by a small amount in the northeastern part than in the remaining regions.

6.3. G10.15–0.34 and G10.30–0.15

These two UC HII regions are located in the W31 HII region/molecular cloud complex. In lower-resolution radio continuum maps, W31 comprises two strong components which contain G10.15–0.34 and G10.30–0.15, respectively. The SNR G10.0–0.3, which was identified as the soft γ -ray repeater SGR 1806–20 (Kulkarni & Frail 1993), is $\sim 9'$ southwest of G10.15–0.34.

Our radio continuum observations show in the field of G10.15–0.34 that there are several compact components including two strong ones and that they are embedded in extended emission of $10.'9 \times 6.'7$ (or $19.0 \times 11.1 \text{ pc}^2$ at 6.0 kpc) (Fig. 1e). The UC HII region lies in the western compact component. The central region is extended in the east-west direction. Based on their VLA continuum observations at 5 GHz, Woodward et al. (1984) suggested that this elongated region consists of about 20 dense ionized clumps and that the individual clumps are HII regions excited by separate embedded stars of spectral types B0.5–O6.5. The surface brightness declines rapidly to the west, while it decreases slowly to the east. As mentioned in § 3.2, our RRL observations strongly suggest that the eastern protuberance may be a result of the champagne flow (Fig. 4).

In the field G10.30–0.15 (Fig 1f), we can see two compact components surrounded by diffuse emission extending over $12.'8 \times 4.'6$ (or $22.3 \times 8.0 \text{ pc}^2$ at 6.0 kpc). The two compact components form

an ionized ridge elongated in the NE-SW direction and the western one contains G10.30–0.15. The diffuse envelope extends straight in the NW-SE direction perpendicular to the central ridge. Such a bipolar HII region can be produced by the champagne flow in the case where the ionizing source is located in a thin, flat molecular cloud (Bodenheimer, Tenorio-Tagle, & Yorke 1979). According to our molecular line observations (Kim & Koo 2000), the distribution of the ambient molecular gas strongly supports the Champagne flow model. However, we could not observe a significant velocity difference between the central region and the envelope. This is presumably because the inclination angle of the extended structure is close to zero. We will present the result of a detailed infrared and radio study on the W31 region in a forthcoming paper (Kim & Koo 2000).

6.4. G23.46–0.20 and G25.72+0.05

These two spherical UC HII regions have no associated compact components. The extended HII region associated with G23.46–0.20 consists of three compact components and a diffuse envelope elongated in the east-west direction (Fig. 1*i*). G23.46–0.20 is located near the edge of the extended HII region. The velocities of the northern and western parts are lower than that of the central region by $\sim 4 \text{ km s}^{-1}$ (see Table 5). G25.72+0.05 is also located on the sky near the edge of an extended HII region with a single compact component (Fig 1*l*) but the velocity of G25.72+0.05 is very different from that of the extended HII region as noted in § 3.2. This strongly suggests that they are a chance coincidence in the line of sight. NH_3 (2,2) lines with almost same velocity ($v_{\text{LSR}} \simeq 100 \text{ km s}^{-1}$) as the H76 α lines were detected towards G23.46–0.20 and G25.72+0.05 (Churchwell et al. 1990a). Thus these two UC HII regions are likely to be real UC HII regions. Their exciting stars were determined to be B0 stars by WC89. However, we can not rule out absolutely the possibility that they may be externally ionized dense clumps, especially in the case of G23.46–0.20.

6.5. G29.96–0.02

G29.96–0.02 is a prototypical cometary UC HII region and has been studied in detail at infrared and radio wavelengths. This UC HII region appears as a $\sim 5''$ diameter edge-brightened arclike structure in the VLA maps of WC89. In order to explain the cometary morphology and velocity structure of this source, two competing models were proposed: the bow shock model (Wood & Churchwell 1991; Mac Low et al. 1991; Afflerbach et al. 1994) and the Champagne flow model (Fey et al. 1995; Pratap, Megeath, & Bergin 1999; Lumsden & Hoare 1999). Recent near-infrared images show that G29.96–0.02 lies in an embedded cluster (Fey et al. 1995; Pratap et al. 1999). Watson & Hanson (1997) restricted the exciting star to spectral classes O5–O8 on the basis of its *K*-band spectrum.

Our radio continuum observations reveal several compact components including two strong ones in this field (Fig. 1*n*). G29.96–0.02 exists in the northern compact component from which

two protuberances stretch to the east and to the southwest, respectively. Most compact components are embedded in extended emission of $6.'3 \times 5.'2$ (or 16.5×13.6 pc² at 9 kpc). There does not exist a significant velocity difference between the compact components and extended envelope, suggesting a physical association between them.

6.6. Other Sources

6.6.1. *G6.55–0.10*

G6.55–0.10, also known as W28 A1, is located on the sky near the center of the W28 SNR, which appears to be an incomplete shell with a diameter of $\sim 30'$ in our radio continuum map (Fig. 1c). The distance to W28 is known to be ~ 2 kpc (Kaspi et al. 1993), whereas G6.55–0.10 seems to be located at a much greater distance of 16.7 kpc on the basis of H₂CO absorption line observations (Downes et al. 1980). Hence, the two objects are not physically associated but happen to lie along the line of sight. G6.55–0.10 appears to be elongated in the north-south direction in Figure 1c (see also Fig. 1 of Andrews et al. 1985). The central velocity of the H76 α line emission from this source is 13.2 km s^{–1}, which is in good agreement with that (~ 15 km s^{–1}) of Andrews et al. (1985) who made high-resolution ($8.''3 \times 4.''0$) H76 α line observations using the VLA.

6.6.2. *G8.14+0.23*

G8.14+0.23 is located at the peak of an extended ($4.'7 \times 3.'4$) structure with a bipolar morphology extended in the north-south direction (Fig. 1d). Such a radio continuum appearance can be interpreted as a result of the champagne flow originating from a thin, flat molecular cloud. The central velocity of the southern protuberance is equal to that of the compact component within 2 km s^{–1}, which is possible if the axis of the extended HII region is in the plane of the sky, similar to G10.30–0.15. Since the surface brightness declines more rapidly on the eastern side than on the western side, the gas density and/or the thickness appear to decrease from the east to the west along the thin molecular cloud. Shepherd & Churchwell (1996) found high-velocity molecular gas, which is suggestive of bipolar outflow, in this object.

6.6.3. *G12.21–0.10*

G12.21–0.10 is embedded in extended emission with three compact components (Fig. 1g). The surface brightness declines slowly to the northeast, while it drops steeply on the other side. G12.21–0.10 appears as a $\sim 4''$ cometary structure in the VLA map of WC89, and is located in the northern compact component in our radio continuum map. The compact components have the same velocity, which is different from that of the northeastern part by ~ 3 km s^{–1}. High-velocity

molecular gas was detected toward this object (Shepherd & Churchwell 1996).

7. Conclusions

We made VLA radio continuum observations of 16 simple UC HII regions with large ratios of S_{SD}/S_{VLA} and detected extended emission towards all the sources. The extended emission consists of one to several compact components and a diffuse envelope. All the UC HII regions except for two spherical ones (G23.46–0.20 and G25.72+0.05) are located in the compact components. There is no significant velocity difference between the ultracompact, compact, and extended components in each source with one exception (G25.72+0.05), which strongly suggests that they are physically associated in almost all of our sources. The UC HII regions always correspond to the peaks of their associated compact components and the compact components with UC HII regions are usually more compact than those without UC HII regions. It is therefore likely that the associated compact components and their immediate envelopes have been produced by UV photons escaping from the UC HII regions, although we can not completely exclude the possibility that they could have been created by separate ionizing sources in a cluster or by sequentially formed massive stars. Consequently, almost all of the UC HII regions in our sample are unlikely to be ‘real’ UC HII regions and their actual ages may be much greater than 10^4 yr. The two UC HII regions with no associated compact components may be ‘real’ UC HII regions or externally ionized dense clumps.

We calculated the ratios of S_{SD}/S_{VLA} for the previously known UC HII regions with simple morphology and found that most of them have large ratios like our sources. Therefore, the age problem of UC HII regions would be significantly alleviated. We presented a simple model in which the presence of extended emission around UC HII regions can be understood using both the Champagne flow model and the hierarchical structure of massive star-forming regions. In our model the UC HII regions and their associated compact and extended components may not represent an evolutionary sequence. The three components could coexist for a long ($>10^5$ yr) time for an HII region which evolves within a hierarchically clumpy molecular cloud. In this context, the compact components without UC HII regions seem to be in a later evolutionary phase than those with UC HII regions. The relation $n_e \propto D^{-1}$ may also be a corollary of the hierarchical structure of molecular clouds.

We thank Dana Balser for his help with the RRL observations and data reduction. We are very grateful to Ed Churchwell and Stan Kurtz for carefully reading the manuscript and for many helpful comments and suggestions. K.-T. K. acknowledges support from Korea Research Foundation grant for junior researcher in 1996. This work has been supported by Korea Science and Engineering Foundation through Grant No. 961-0203-014-02, and also BK21 Program, Ministry of Education, Korea through SEES.

REFERENCES

- Afflerbach, A., Churchwell, E., Hofner, P., & Kurtz, S. 1994, *ApJ*, 437, 697
- Afflerbach, A., Churchwell, E., Accord, J. M., Hofner, P., Kurtz, S., & Depree, C. G. 1996, *ApJS*, 106, 423
- Andrews, M. D., Basart, J. P., & Lamb, R. C. 1985, *AJ*, 90, 310
- Bodenheimer, P., Tenorio-Tagle, G., & Yorke, H. W. 1979, *ApJ*, 233, 85
- Cesaroni, R., Walmsley, C. M., & Churchwell, E. 1992, *A&A*, 256, 618
- Cesaroni, R., Churchwell, E., Hofner, P., & Walmsley, C. M. 1994, *A&A*, 288, 903
- Chaisson, E. J., Lichten, S. M., & Rodríguez, L. F. 1978, *ApJ*, 221, 810
- Churchwell, E. 2000, in *The Origin of Stars and Planetary Systems*, ed. C. J. Lada & N. D. Kylafis (Dordrecht: Kluwer), 515
- Churchwell, E., Walmsley, C. M., & Cesaroni, R. 1990a, *A&AS*, 83, 119
- Churchwell, E., Walmsley, C. M., Wood, D. O. S., & Steppe, H. 1990b, in *Radio Recombination Lines: 25 Years of Investigations*, ed. M. A. Gordon & R. L. Sorochenko (Dordrecht: Kluwer), 83
- Codella, C., Felli, M., & Natale, V. 1994, *A&A*, 284, 233
- De Pree, C. G., Rodríguez, L. F., & Goss, W. M. 1995, *Rev. Mexicana Astron. Astrofis.*, 31, 39
- Downes, D., Wilson, T. L., Bieging, J., & Wink, J. 1980, *A&AS*, 40, 379
- Elmegreen, B. G., & Lada, C. J. 1977, *ApJ*, 214, 725
- Elliot, K. H., Goudis, C., Hippelein, H., & Meaburn, J. 1984, *A&A*, 138, 451
- Fey, A. L., Gaume, R. A., Claussen, M. J., & Vrba, F. J. 1995, *ApJ*, 453, 308
- Forster, J. R., Caswell, J. L., Okumura, S. K., Hasegawa, T., & Ishiguro, M. 1990, *A&A*, 231, 473
- Fürst, E., Reich, W., Reich, P., & Reif, K. 1990, *A&AS*, 85, 805
- Garay, G., & Lizano, S. 1999, *PASP*, 111, 1049
- Garay, G., & Rodríguez, L. 1983, *ApJ*, 266, 263
- Garay, G., & Rodríguez, L. 1990, *ApJ*, 362, 191
- Garay, G., Rodríguez, L., Moran, J. M., & Churchwell, E. 1993, *ApJ*, 418, 368
- García-Segura, G., & Franco, J. 1996, *ApJ*, 469, 171
- Habing, H. J., & Israel, F. P. 1979, *ARA&A*, 17, 345
- Kaspi, V. M., Lyne, A. G., Manchester, R. N., Johnston, S., D'amico, N., & Shemar, S. L. 1993, *ApJ*, 409, L57
- Kim, K.-T., & Koo, B.-C. 1996, *J. Korean Astron. Soc.*, 29, S177

- Kim, K.-T., & Koo, B.-C. 2000, in preparation
- Koo, B.-C., Kim, K.-T., Lee, H.-G., Yun, M.-S., & Ho, P. T. 1996, *ApJ*, 456, 662
- Kulkarni, S. R., & Frail, D. A. 1993, *Nature*, 365, 33
- Kurtz, S., Cesaroni, R., Churchwell, E., Hofner, P., & Walmsley, C. M. 2000, in *Protostars and Planets IV*, ed. V. Mannings, A. Boss, & S. Russell (Tucson: Univ. Arizona Press), 299
- Kurtz, S., Churchwell, E., & Wood, D. O. S. 1994, *ApJS*, 91, 659 (KCW)
- Kurtz, S., Watson, A. M., Hofner, P., & Otte, B. 1999, *ApJ*, 514, 232
- Lada, C. J., Gull, T. R., Gottlieb, C. A., & Gottlieb, E. W. 1976, *ApJ*, 203, 159
- Lockman, F. J. 1989, *ApJS*, 71, 469
- Lumsden, S. L., & Hoare, M. G. 1999, *MNRAS*, 305, 701
- Mac Low, M.-M., van Buren, D., Wood, D. O. S., & Churchwell, E. 1991, *ApJ*, 369, 395
- Mezger, P. G. 1980, in *Proc. Workshop on Recombination Lines*, ed. P. A. Shaver (Dordrecht: Reidel), 81
- Panagia, N. 1973, *AJ*, 78, 928
- Panagia, N., & Walmsley, C. M. 1978, *A&A*, 70, 411
- Plume, R., Jaffe, D. T., & Evans, N. J. II 1992, *ApJS*, 78, 505
- Plume, R., Jaffe, D. T., Evans, N. J. II, Martín-Pintado, J., & Gómez-González, J 1997, *ApJ*, 476, 730
- Pratap, P., Megeath, S. T., & Bergin, E. A. 1999, *ApJ*, 517, 799
- Rubin, R. H. 1968, *ApJ*, 154, 391
- Schraml, J., & Mezger, P. G. 1969, *ApJ*, 156, 269
- Shaver, P. A., McGee, R. X., Newton, L. M., Danks, A. C., & Pottasch, S. R. 1983, *MNRAS*, 204, 53
- Shepherd, D. S., & Churchwell, E. 1996, *ApJ*, 472, 225
- Snell, R. L., Goldsmith, P. F., Erickson, N. R., Mundy, L. G., & Evans, N. J. II 1984, *ApJ*, 276, 625
- Spitzer, L. Jr. 1968, *Diffuse Matter in Space* (New York: Interscience Publishers), 183
- Stecklum, B., Henning, T., Feldt, M., Hayward, T. L., Hoare, M. G., Hofner, P., & Richter, S. 1998, *AJ*, 115, 767
- Stutzki, J., & Güsten, R. 1990, *ApJ*, 356, 513
- Stutzki, J., Stacey, G. J., Genzel, R., Harris, A. I., Jaffe, D. T., & Lugten, J. B. 1988, *ApJ*, 332, 379
- Sung, H., Chun, M.-Y., & Bessell, M. S. 2000, *AJ*, 120, 333

- Tenorio-Tagle, G. 1982, in *Regions of Recent Star Formation*, ed. R. S. Roger & P. E. Dewdney (Dordrecht: Kluwer), 1
- Watson, A. M., & Hanson, M. M. 1997, *ApJ*, 490, L165
- Wink, J. E., Altenhoff, W. J., & Mezger, P. G. 1982, *A&A*, 108, 227
- Wood, D. O. S., & Churchwell, E. 1989a, *ApJS*, 69, 831 (WC89)
- Wood, D. O. S., & Churchwell, E. 1989b, *ApJ*, 340, 265
- Wood, D. O. S., & Churchwell, E. 1991, *ApJ*, 372, 199
- Woodward, C. E., Helfer, H. L., & Pipher, J. L. 1984, *MNRAS*, 209, 209
- Wolf, N. J. 1961, *PASP*, 73, 206
- Zijlstra, A. A., Pottasch, S. R., Engels, D., Roelfsema, P. R., Hekkert, P. Te-Lintel, & Umana, G 1990, *MNRAS*, 246, 217

Table 1. PARAMETERS OF VLA 21 CM CONTINUUM OBSERVATIONS

Parameter	Value
Observation dates	1995 Feb 11, 13, 14, & 17
Total time	19 hours
Configuration	DnC
Number of antennas	27
Center frequency	1.38510 & 1.46490 GHz
Bandwidth	50 MHz
Largest structure visible	15'
Synthesized beam FWHM	$\sim 40'' \times 20''$
Primary beam FWHM	30'
Flux calibrator source	3C286
Phase calibrator source	1819-096
Typical on-source time	40 minutes
Number of fields observed	16
Typical rms noise	1 mJy beam ⁻¹

Table 2. OBSERVATIONAL PARAMETERS OF 16 UC HII REGIONS FOR VLA 21 CM CONTINUUM OBSERVATIONS

Source	Phase Center		ON-source Time (minute)	Synthesized FWHM (")	RMS noise of Image (mJy beam ⁻¹)	Adopted ^a Distance (kpc)	Morphology ^b of UC HII Region
	$\alpha(1950)$	$\delta(1950)$					
G5.89–0.39	17 ^h 57 ^m 26 ^s .8	–24°03′56″	40	39 × 27	1.70	2.6	shell
G5.97–1.17	18 00 36.4	–24 22 54	35	40 × 28	2.75	1.9	core-halo
G6.55–0.10	17 57 47.4	–23 20 30	35	42 × 25	2.50	16.7	irregular
G8.14+0.23	18 00 00.2	–21 48 15	35	50 × 22	0.53	4.2	irregular
G10.15–0.34	18 06 22.5	–20 20 05	40	37 × 25	1.71	6.0	irregular
G10.30–0.15	18 05 57.9	–20 06 26	40	37 × 25	1.62	6.0	cometary
G12.21–0.10	18 09 43.7	–18 25 09	40	38 × 24	0.49	16.1	cometary
G12.43–0.05	18 09 58.9	–18 11 58	40	40 × 24	0.90	16.7	cometary
G23.46–0.20	18 32 01.2	–08 33 33	45	40 × 18	0.91	9.0	spherical
G23.71+0.17	18 31 10.3	–08 09 36	45	40 × 18	0.73	9.0	core-halo
G23.96+0.15	18 31 42.6	–07 57 11	60	40 × 18	0.60	6.0	irregular
G25.72+0.05	18 35 21.6	–06 26 27	55	41 × 18	0.85	14.0	spherical
G27.28+0.15	18 37 55.7	–05 00 35	60	40 × 17	0.65	15.2	irregular
G29.96–0.02	18 43 27.1	–02 42 36	50	44 × 18	1.62	9.0	cometary
G35.05–0.52	18 54 37.1	+01 35 01	35	44 × 17	1.37	12.7	irregular
G37.55–0.11	18 57 46.8	+03 58 55	35	44 × 17	0.61	12.0	core-halo

^aFrom references given by Wood & Churchwell (1989)

^bWood & Churchwell (1989)

Table 3. 21 CM CONTINUUM PARAMETERS OF 16 UC HII REGIONS

Source	Peak Position		Extent ^a		Peak Brightness (Jy beam ⁻¹)	Integrated Flux Density (Jy)
	$\alpha(1950)$	$\delta(1950)$	Angular (square arcmin)	Linear (pc ²)		
G5.89–0.39	17 ^h 57 ^m 37. ^s 7	–24°03′51″	14.4 × 9.0	10.9 × 6.8	0.91	20.86
A	17 57 37.7	–24 04 08	1.58 × 1.38	1.20 × 1.05	0.91	7.79
B [†]	17 57 27.3	–24 04 13	1.09 × 0.79	0.82 × 0.60	0.32	1.30
G5.97–1.17	18 00 36.8	–24 22 49	14.5 × 10.7	8.0 × 5.9	3.57	48.29
A [†]	18 00 36.6	–24 22 48	1.24 × 1.14	0.69 × 0.63	2.69	14.93
G6.55–0.10	17 57 47.0	–23 20 25	3.5 × 2.2	17.0 × 10.7	1.07	2.32
A [†]	17 57 47.0	–23 20 24	0.55 × 0.48	2.67 × 2.33	1.03	2.06
G8.14+0.23	18 00 00.9	–21 48 15	6.9 × 2.8	8.4 × 3.4	2.04	6.67
A [†]	18 00 00.5	–21 48 13	0.75 × 0.57	0.92 × 0.70	1.74	4.71
G10.15–0.34	18 06 27.8	–20 20 00	10.9 × 6.7	19.0 × 11.7	2.94	55.22
A	18 06 27.5	–20 19 59	1.75 × 1.08	3.05 × 1.88	2.77	23.20
B [†]	18 06 22.0	–20 20 00	1.57 × 0.48	2.74 × 0.84	2.24	9.94
G10.30–0.15	18 06 02.1	–20 05 41	12.8 × 4.6	22.3 × 8.0	1.42	15.92
A	18 06 02.5	–20 05 31	1.28 × 0.76	2.23 × 1.33	1.32	6.63
B [†]	18 05 57.8	–20 06 19	0.93 × 0.63	1.62 × 1.10	1.03	3.53
G12.21–0.10	18 09 42.0	–18 26 05	4.7 × 3.4	22.0 × 15.9	0.32	3.06
A	18 09 42.1	–18 25 59	0.56 × 0.47	2.65 × 2.19	0.32	0.67
B	18 09 47.7	–18 26 33	1.25 × 0.82	5.85 × 3.82	0.24	1.27
C [†]	18 09 44.0	–18 25 15	0.85 × 0.46	3.98 × 2.19	0.18	0.46
G12.43–0.05	18 09 58.9	–18 11 58	3.0 × 2.2	14.6 × 10.7	0.14	0.69
A [†]	18 09 58.7	–18 11 56	1.02 × 0.78	4.95 × 3.79	0.11	0.45
G23.46–0.20	18 32 00.5	–08 34 43	8.8 × 5.8	23.0 × 15.2	0.41	11.31
A	18 32 00.7	–08 34 48	1.98 × 0.88	5.18 × 2.30	0.37	3.47
B	18 32 01.1	–08 36 10	3.47 × 1.35	9.08 × 3.53	0.28	6.80
G23.71+0.17	18 31 10.0	–08 09 41	2.9 × 1.8	7.6 × 4.7	0.46	1.93
A [†]	18 31 10.0	–08 09 50	0.95 × 0.57	2.49 × 1.49	0.44	1.85
G23.96+0.15	18 31 42.2	–07 57 11	3.1 × 1.5	5.4 × 2.6	1.08	2.13
A [†]	18 31 42.1	–07 57 10	0.43 × 0.25	0.75 × 0.44	1.02	1.71
G25.72+0.05	18 35 22.9	–06 28 12	3.2 × 2.5	13.0 × 10.2	0.18	1.74
A	18 35 22.3	–06 28 04	1.43 × 1.11	5.82 × 4.52	0.16	1.43
G27.28+0.15	18 37 55.7	–05 00 35	2.6 × 1.4	11.5 × 6.2	0.44	0.96
A [†]	18 37 55.7	–05 00 35	0.57 × 0.29	2.52 × 1.28	0.40	0.74
G29.96–0.02	18 43 27.4	–02 42 36	6.3 × 5.2	16.5 × 13.6	1.50	12.69
A [†]	18 43 27.4	–02 42 34	0.40 × 0.37	1.05 × 0.97	1.36	2.61
B	18 43 32.6	–02 44 57	1.47 × 1.23	3.85 × 3.22	0.61	6.08
G35.05–0.52	18 54 31.8	+01 34 26	3.7 × 3.1	13.7 × 11.5	0.19	1.64
A [†]	18 54 37.0	+01 34 56	0.43 × 0.27	1.59 × 1.00	0.17	0.27
B	18 54 31.9	+01 34 44	1.56 × 1.02	5.76 × 3.77	0.14	1.37
G37.55–0.11	18 57 46.8	+03 58 55	2.1 × 1.8	7.3 × 6.3	0.45	1.12
A [†]	18 57 46.8	+03 58 53	0.54 × 0.46	1.88 × 1.61	0.39	0.96

[†]Compact component that contains an UC HII region

^aDeconvolved diameters at half-maximum for compact components, while diameters at 10 mJy beam⁻¹ for extended envelopes

Table 4. PHYSICAL PARAMETERS OF 16 UC HII REGIONS

Source	n_e (cm^{-3})	EM (10^4 pc cm^{-6})	U (pc cm^{-2})	M_{HII} (M_{\odot})	$\log N'_c$ (s^{-1})	Spectral ^a Type	f_d (%)	$T_e^{*\text{b}}$ (K)
G5.89–0.39	64	3.5	69.1	480	49.08	O6 (O7)	95	8500
A	473	36.9	50.0	25	48.66	O7		
B [†]	391	15.7	27.4	5	47.88	O9.5		
G5.97–1.17	98	6.6	73.3	380	49.20	O6 (B0)	~0	7700
A [†]	1036	103.9	49.6	11	48.69	O7		
G6.55–0.10	66	6.0	111.7	1970	49.80	O4.5 (O8.5)	34	6700
A [†]	443	72.5	107.3	262	49.75	O4.5		
G8.14+0.23	111	6.6	62.0	200	49.10	O6 (B0)	~0	5600
A [†]	917	98.3	55.2	17	48.95	O6.5		
G10.15–0.34	99	14.5	158.7	3800	50.33	>O4 (O8)	59	5500
A	555	108.3	118.9	285	49.95	O4		
B [†]	726	116.8	89.6	93	49.58	O5		
G10.30–0.15	64	5.5	107.5	1820	49.74	O4.5 (O8.5)	73	6800
A	505	64.5	80.2	96	49.36	O5.5		
B [†]	540	57.2	65.0	48	49.09	O6		
G12.21–0.10	46	3.9	120.2	3550	49.88	O4 (O6.5)	88	7000
A	261	24.2	72.4	137	49.22	O5.5		
B	136	11.9	89.6	518	49.50	O5		
C [†]	160	11.0	63.9	153	49.05	O6		
G12.43–0.05	44	2.4	78.2	1030	49.19	O6 (O9)	~0	10000
A [†]	99	6.2	68.0	297	49.00	O6		
G23.46–0.20	49	4.5	124.6	3700	49.96	O4 (B0)	49	6300
A	191	18.4	84.0	292	49.45	O5.5		
B	126	13.3	105.1	864	49.74	O5		
G23.71+0.17	112	7.6	70.1	290	49.17	O6 (O9)	38	7100
A [†]	341	32.8	69.0	91	49.15	O6		
G23.96+0.15	145	8.1	53.1	100	48.93	O6.5 (O9.5)	42	5100
A [†]	1299	140.0	49.4	9	48.84	O6.5		
G25.72+0.05	63	4.5	90.2	1100	49.52	O5 (B0)	35	6700
A	106	8.5	84.5	534	49.43	O5.5		
G27.28+0.15	82	5.7	79.5	570	49.30	O5.5 (O9.5)	48	7700
A [†]	418	45.5	72.9	87	49.19	O6		
G29.96–0.02	71	7.5	128.2	2780	50.03	O4 (O5.5)	85	5800
A [†]	1022	155.7	75.7	40	49.34	O5.5		
B	241	30.1	100.3	393	49.71	O5		
G35.05–0.52	50	3.1	84.8	1160	49.37	O5.5 (O9)	83	8100
A [†]	356	23.5	46.7	27	48.59	O7		
B	112	8.7	79.9	426	49.29	O5.5		
G37.55–0.11	96	6.1	69.5	330	49.21	O6 (O7.5)	52	6100
A [†]	376	35.9	66.0	72	49.15	O6		

[†]Compact component that contains an UC HII region

^aSpectral types measured from UC HII regions alone are given in parentheses

^bTaken from Downes et al. (1980) and Wink et al. (1982)

Table 5. H76 α LINE PARAMETERS OF UC HII REGIONS

Source	Observed Position		v_{LSR} (km s $^{-1}$)	T_{L} (mK)	Δv (km s $^{-1}$)	$\int T_{\text{L}} dv$ (mK km s $^{-1}$)
	$\alpha(1950)$	$\delta(1950)$				
G5.89–0.39 ^a	17 ^h 57 ^m 26 ^s .8	–24°03′56″				
	(00 ^s .0, 00′00″) ^o		9.9±0.4	95±1.4	54.8±1.0	5484
	(–13.4, 00 00)		15.0±0.8	25±1.3	30.7±1.9	771
	(–05.4, 00 00)		13.5±0.7	29±1.7	22.9±1.5	684
	(+02.6, 00 00) ^o		4.6±0.5	95±1.7	53.5±1.1	5436
	(+10.6, –04 00)		15.0±0.5	34±1.7	19.7±1.1	757
	(+10.6, –02 00)		12.3±0.2	56±1.2	21.1±0.5	1253
	(+10.6, 00 00) [•]		10.4±0.1	144±1.5	24.7±0.3	3955
	(+10.6, +02 00)		11.7±0.3	55±1.5	23.3±0.7	1404
	(+10.6, +04 00)		10.7±0.7	26±1.5	26.1±1.7	709
	(+18.6, 00 00) ^o		9.8±0.2	122±1.8	26.7±0.4	3594
	(+26.6, 00 00)		13.5±0.5	43±1.7	23.8±1.1	1083
	(+34.6, 00 00)		8.1±0.6	33±1.9	20.9±1.4	739
	(+42.6, 00 00)			≤ 7		
G5.97–1.17 ^a	18 00 36.4	–24 22 54				
	(00.0, 00 00) [•]		4.5±0.1	279±1.7	26.8±0.2	7856
	(–24.0, 00 00)		3.3±0.4	37±1.6	20.2±1.0	789
	(–16.0, 00 00)		2.4±0.3	67±1.7	22.5±0.7	1568
	(–08.0, 00 00)		2.5±0.2	120±1.8	23.1±0.4	2976
	(00.0, –06 00)		5.0±0.5	40±2.0	19.7±1.1	874
	(00.0, –04 00)		4.5±0.2	61±1.3	20.0±0.5	1236
	(00.0, –02 00) ^o		3.8±0.2	120±1.8	24.7±0.4	3183
	(00.0, +02 00) ^o		2.3±0.1	185±1.9	25.0±0.3	4906
	(00.0, +04 00)		1.5±0.2	80±1.8	22.0±0.6	1827
	(00.0, +06 00)		–0.2±0.5	46±1.9	24.1±1.2	1244
	(+08.0, 00 00)		4.6±0.1	129±1.3	25.2±0.3	3420
	(+16.0, 00 00)		6.9±0.2	91±1.6	21.1±0.4	2140
	(+24.0, 00 00)		7.8±0.3	62±1.8	22.7±0.8	1492
	(+32.0, 00 00)		5.0±0.7	40±2.4	22.2±1.5	865
	(+40.0, 00 00)		3.0±0.4	60±2.0	21.8±0.8	1456
	(+08.0, –04 00)		3.4±0.3	60±1.9	18.9±0.7	1182
	(+16.0, –04 00)		1.6±0.2	85±1.4	22.1±0.4	2002
	(+24.0, –04 00)		0.5±0.3	80±2.1	19.9±0.6	1669
(+32.0, –04 00)		1.8±0.5	46±1.8	30.0±1.2	1341	
(+40.0, –04 00)		1.3±0.5	44±2.0	21.8±1.2	976	
G6.55–0.10	17 57 47.4	–23 20 30				
	(00.0, 00 00)		13.2±0.4	70±1.9	26.5±0.8	2025
G8.14+0.23	18 00 00.2	–21 48 15				
	(00.0, 00 00)		20.3±0.4	58±1.6	27.3±0.9	1700
	(+06.4, –01 10)		22.2±1.1	19±1.8	22.2±2.5	405

Table 5—Continued

Source	Observed Position		v_{LSR} (km s^{-1})	T_{L} (mK)	Δv (km s^{-1})	$\int T_{\text{L}} dv$ (mK km s^{-1})
	$\alpha(1950)$	$\delta(1950)$				
G10.15–0.34	18 06 22.5	–20 20 05				
	(00.0, 00 00) [•]		16.4±0.2	163±2.3	29.7±0.5	5170
	(–10.8, 00 00)		23.5±0.9	48±1.9	47.5±2.1	2193
	(–05.8, +02 00) [◦]		14.6±0.2	190±2.0	35.8±0.5	7473
	(–02.8, –02 00)		13.5±0.9	18±0.2	16.5±2.0	344
	(–02.8, 00 00)		16.2±0.1	254±2.1	32.5±0.3	8819
	(00.0, +05 00)		14.3±0.6	30±1.4	26.1±1.4	859
	(+03.8, +02 25) [•]		15.4±0.2	306±3.1	32.1±0.4	10598
	(+05.2, –04 00)			≤8		
	(+05.2, –02 00)		11.0±0.5	47±1.6	31.3±1.2	1517
	(+05.2, +00 10) [•]		14.6±0.1	352±2.4	32.0±0.4	12226
	(+06.3, –05 40)		15.0±0.3	40±1.3	19.6±0.7	806
	(+13.2, –02 00)		18.4±0.6	55±1.5	42.9±1.3	2419
	(+13.8, 00 00)		10.3±0.1	189±1.2	32.7±0.3	6712
	(+22.7, –00 10)		4.5±0.4	37±1.4	22.6±1.0	840
(+30.4, 00 00)		4.0±0.9	21±1.8	19.9±2.1	567	
G10.30–0.15	18 05 57.9	–20 06 26				
	(00.0, 00 00)		7.7±0.5	49±1.6	28.5±1.1	1479
	(–06.8, +02 10)		11.9±0.4	31±1.2	23.0±1.0	833
	(+03.5, –01 55)		8.1±0.5	38±1.3	25.7±1.1	1006
(+04.2, +00 50) [•]		11.1±0.2	122±1.9	29.7±0.5	3772	
G12.21–0.10	18 09 43.7	–18 25 09				
	(–01.0, –00 20) ^b		28.9±0.4	31±1.1	22.2±0.9	787
	(+04.2, –01 25)		27.8±0.4	40±1.7	19.5±0.9	960
(+05.6, +00 45)		25.3±0.4	32±1.7	17.0±1.0	545	
G12.43–0.05	18 09 58.9	–18 11 58				
	(00.0, 00 00)			≤7		
G23.46–0.20	18 32 01.2	–08 33 33				
	(00.0, 00 00)		99.0±0.3	54±2.0	16.7±0.8	912
	(–10.8, –02 00)		99.9±0.3	52±1.5	21.5±0.7	1166
	(–04.7, +00 30)		98.7±0.3	47±1.7	16.3±0.7	852
	(–01.3, –03 00)		103.7±0.3	54±1.4	21.8±0.7	1224
	(–00.8, –02 00) [•]		103.1±0.2	126±1.6	24.4±0.4	3293
	(00.0, –01 10)		103.3±0.2	103±0.2	23.0±0.5	2508
	(+09.1, –02 00)		105.2±1.8	48±1.8	19.7±0.9	984
(+27.0, –02 05)			≤6			
G23.71+0.17	18 31 10.3	–08 09 36				
	(00.0, 00 00)		103.0±0.6	39±1.7	30.3±1.5	1292
G23.96+0.15	18 31 42.6	–07 57 11				
	(00.0, 00 00)		78.9±0.5	49±1.7	28.0±1.2	1295
G25.72+0.05	18 35 21.6,	–06 26 27				
	(00.0, 00 00)		98.3±1.9	12±1.5	30.9±4.6	405
	(+01.3, –01 45)		54.1±0.4	32±1.0	27.8±1.0	948

Table 5—Continued

Source	Observed Position		v_{LSR} (km s ⁻¹)	T_{L} (mK)	Δv (km s ⁻¹)	$\int T_{\text{L}} dv$ (mK km s ⁻¹)
	$\alpha(1950)$	$\delta(1950)$				
G27.28+0.15	18 37 55.7	-05 00 35				
	(00.0, 00 00)		35.0±0.8	20±1.3	23.9±1.9	472
G29.96-0.02	18 43 27.1	-02 42 36				
	(00.0, 00 00) [•]		95.9±0.2	115±1.7	28.6±0.6	3730
	(-08.0, -03 05)		98.9±0.2	68±1.4	22.7±0.6	1667
	(-01.7, -06 15)		98.0±0.3	44±1.1	23.7±0.7	1122
	(-00.6, -04 45)		99.1±0.4	54±1.7	24.4±1.0	1388
	(-00.6, -03 15) [•]		100.0±0.3	121±2.5	26.4±0.7	3714
	(-00.6, -01 37) [°]		98.8±0.2	81±1.3	25.6±0.5	2196
	(+05.6, -01 55) [•]		100.4±0.2	133±1.8	26.3±0.4	3646
	(+07.6, -03 10) [°]		101.4±0.2	114±1.6	27.5±0.5	3346
G35.05-0.52	18 54 37.1	+01 35 01				
	(00.0, 00 00)		51.2±0.4	26±1.1	17.9±0.9	470
	(-08.0, +00 55)		50.0±0.7	17±1.5	16.9±1.7	339
	(-05.7, -00 25)		52.0±0.4	21±0.1	17.9±1.0	388
	(-02.9, -00 13)		52.7±0.4	31±1.2	18.9±0.8	600
G37.55-0.11	18 57 46.8,	+03 58 55				
	(00.0, 00 00)		51.5±0.5	28±0.1	30.0±1.3	858

[°]Position where He76 α line emission was observed but not detected ($T_{\text{L}} \lesssim 6$ mK)

[•]Position where He76 α line emission was detected (see Table 6)

^aMapped sources for which part of spectra were presented

^bUC HII region is located within the beam

Table 6. He76 α LINE PARAMETERS OF UC HII REGIONS

Source	Offsets ^a	v_{LSR} (km s ⁻¹)	T_{L} (mK)	Δv (km s ⁻¹)	$\int T_{\text{L}} dv$ (mK km s ⁻¹)	Y ⁺
G5.89–0.39	(+10 ^s 6, 00'00'')	9.8±0.7	11±1.7	8.5±1.6	81	0.020
G5.97–1.17	(00.0, 00 00)	1.5±0.6	21±2.1	12.1±1.4	275	0.035
G10.15–0.34	(00.0, 00 00)	12.3±1.5	12±2.8	13.2±3.5	179	0.035
	(+03.8, +02 25)	14.5±1.4	11±1.9	15.2±3.2	170	0.016
	(+05.2, +00 10)	11.2±0.6	29±2.0	19.7±1.5	593	0.049
G10.30–0.15	(+04.2, +00 50)	15.3±1.2	16±2.6	14.6±2.8	237	0.063
G23.46–0.20	(–00.8, –02 00)	104.1±1.5	14±2.2	18.7±3.5	262	0.080
G29.96–0.02	(00.0, 00 00)	97.1±0.7	13±0.8	21.4±1.7	254	0.068
	(–00.6, –03 15)	103.5±0.8	12±1.0	21.3±1.9	283	0.076
	(+05.6, –01 55)	104.9±0.9	16±1.9	16.6±2.2	250	0.069

^aSame as in Table 5

NOTE. Among the 18 observed positions (Table 5), He76 α line emission was not detected ($T_{\text{L}} \lesssim 6$ mK) at 8 positions

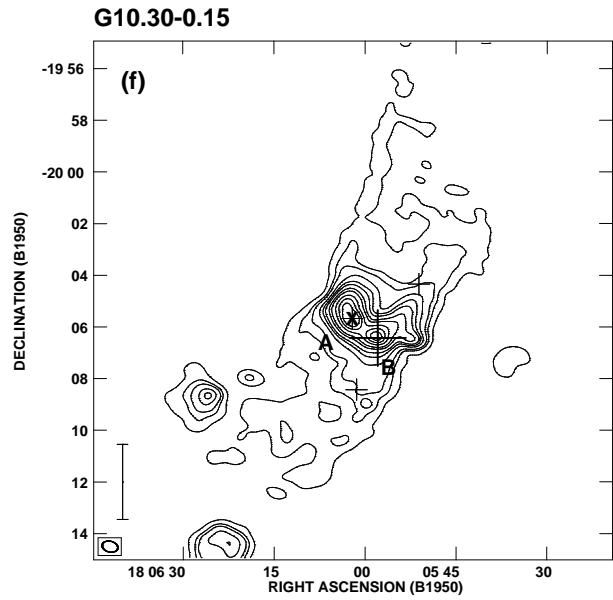
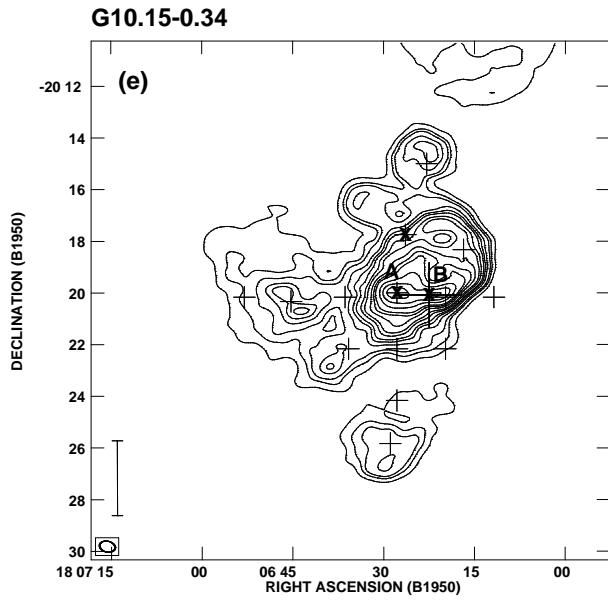
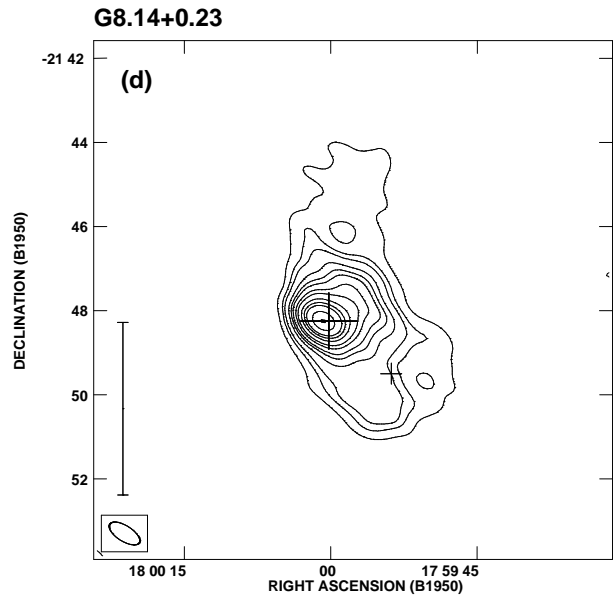
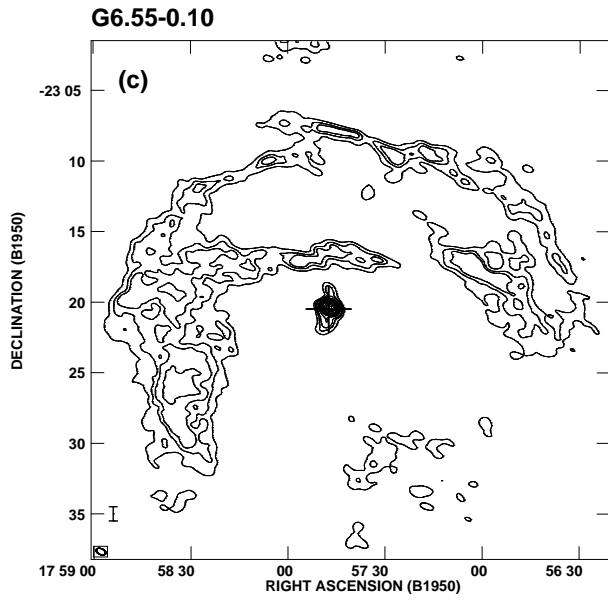
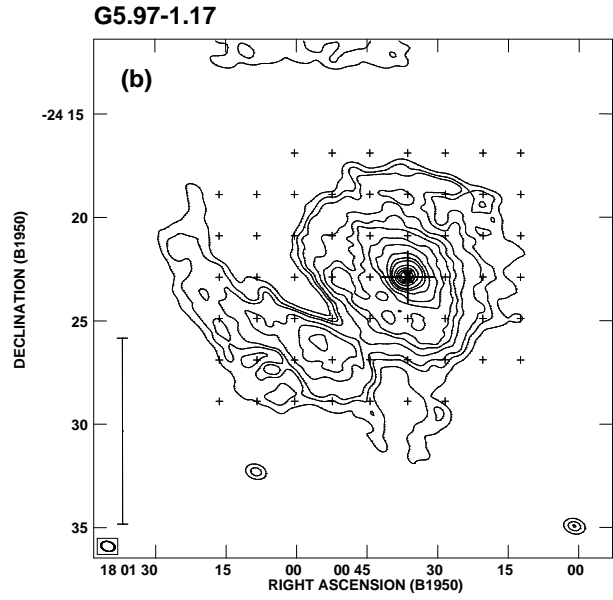
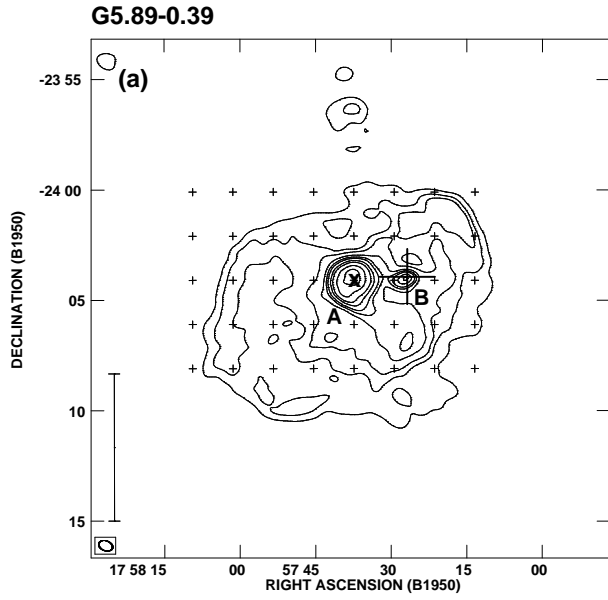
Table 7. RADIO RECOMBINATION AND MOLECULAR LINES OF UC HII REGIONS

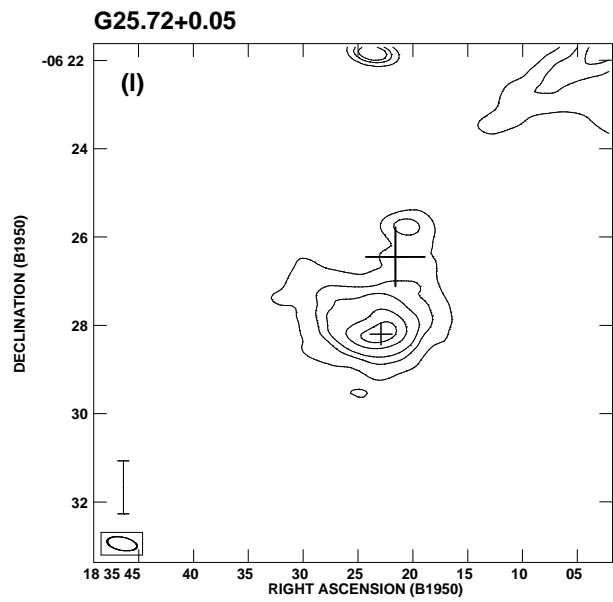
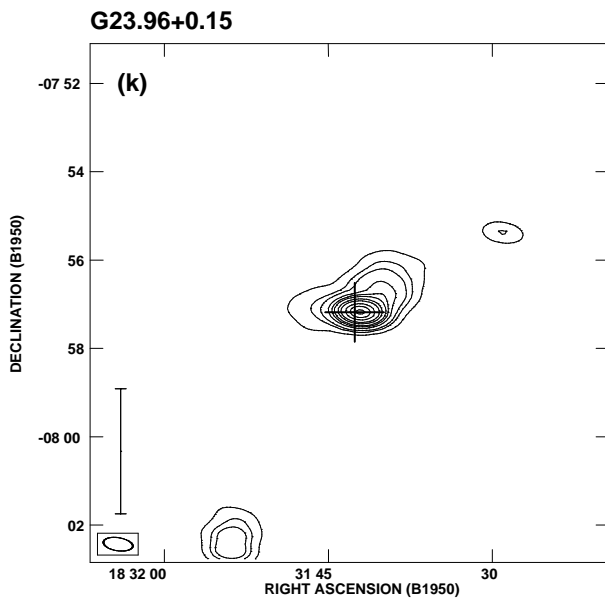
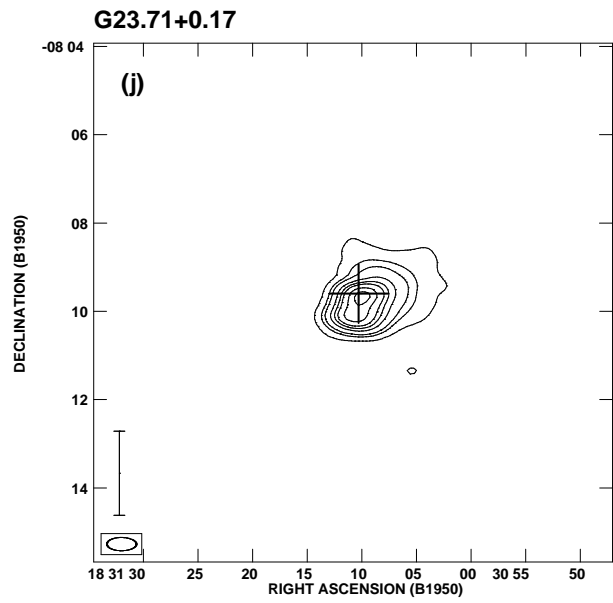
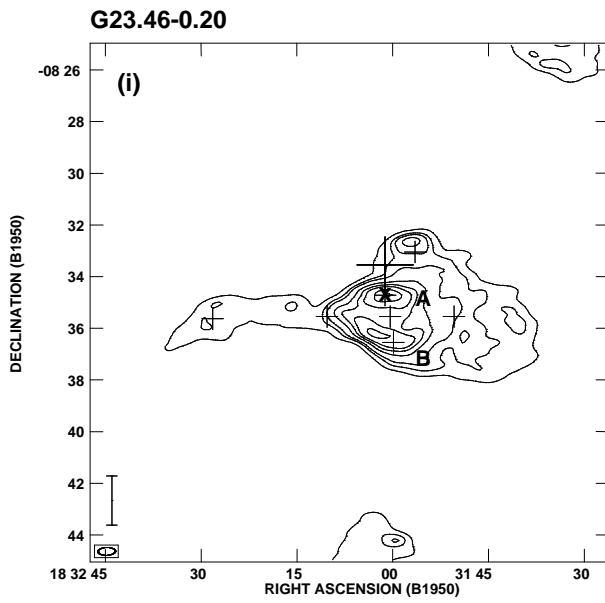
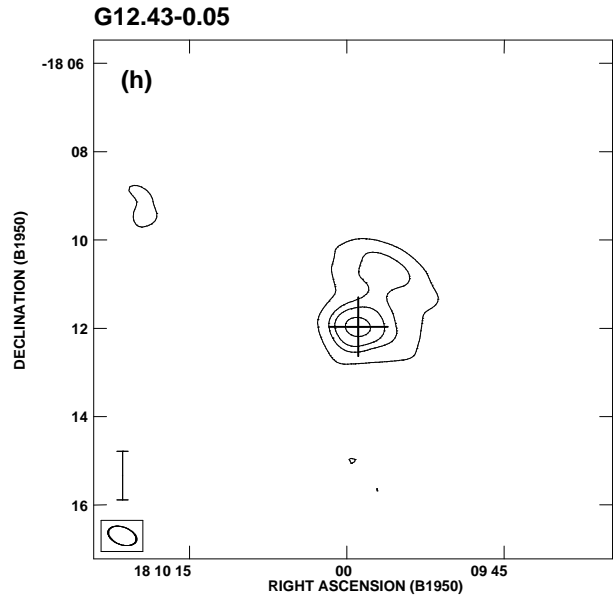
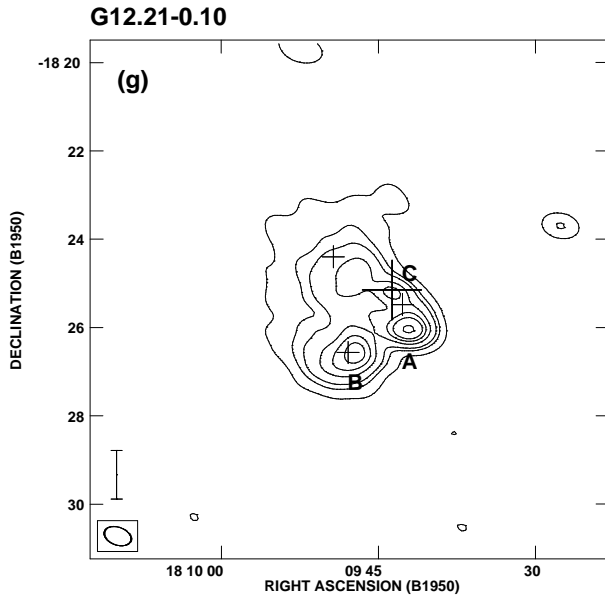
Source	Compact Component ^a		UC HII Region				Reference
	v_{LSR} (km s ⁻¹)	Δv (km s ⁻¹)	RRL (km s ⁻¹)	CS (7–6) (km s ⁻¹)	NH ₃ (2,2) (km s ⁻¹)	NH ₃ (4,4) (km s ⁻¹)	
G5.89–0.39	9.9	54.8	4.9	9.8	9.3	11.0	1, 5, 6, 7
G5.97–1.17	4.5	26.8	9.6	...	6
G6.55–0.10	13.2	26.5	~15	...	12.8	...	2, 6
G8.14+0.23	20.3	27.3	...	18.6	19.3	20.3	5, 6
G10.15–0.34	16.4	29.7	9.9	...	6
G10.30–0.15	7.7	28.5	13.2	12.7	6, 7
G12.21–0.10	28.9	22.2	27.6	23.7	24.3	24.7	3, 5, 6, 7
G12.43–0.05	20.8	...	6
G23.71+0.17	103.0	30.3	113.0	114.6	6, 7
G23.96+0.15	78.9	28.0	73.7	80.4	79.7	...	1, 5, 6
G27.28+0.15	35.0	23.9	31.5	...	6
G29.96–0.02	95.9	28.6	95.6	97.7	97.6	98.1	4, 5, 6, 7
G35.05–0.52	51.2	17.9	49.4	...	6
G37.55–0.11	51.5	30.3	~52 ^b	...	6
$\langle v_{\text{LSR,UC}} - v_{\text{LSR,C}} \rangle$			-2.0±3.0	-0.6±2.9	0.4±4.5	2.7±5.4	

^aH76 α data from this work

^bNH₃ (1,1) data from Churchwell et al. (1990a)

REFERENCES.—(1) H76 α data from Churchwell et al. 1990b. (2) H76 α data from Andrews et al. 1985. (3) H93 α data from Afflerbach et al. 1996. (4) H76 α data from Afflerbach et al. 1994. (5) CS (7–6) data from Plume et al. 1992. (6) NH₃ (2,2) data from Churchwell et al. 1990a. (7) NH₃ (4,4) data from Cesaroni et al. 1992.





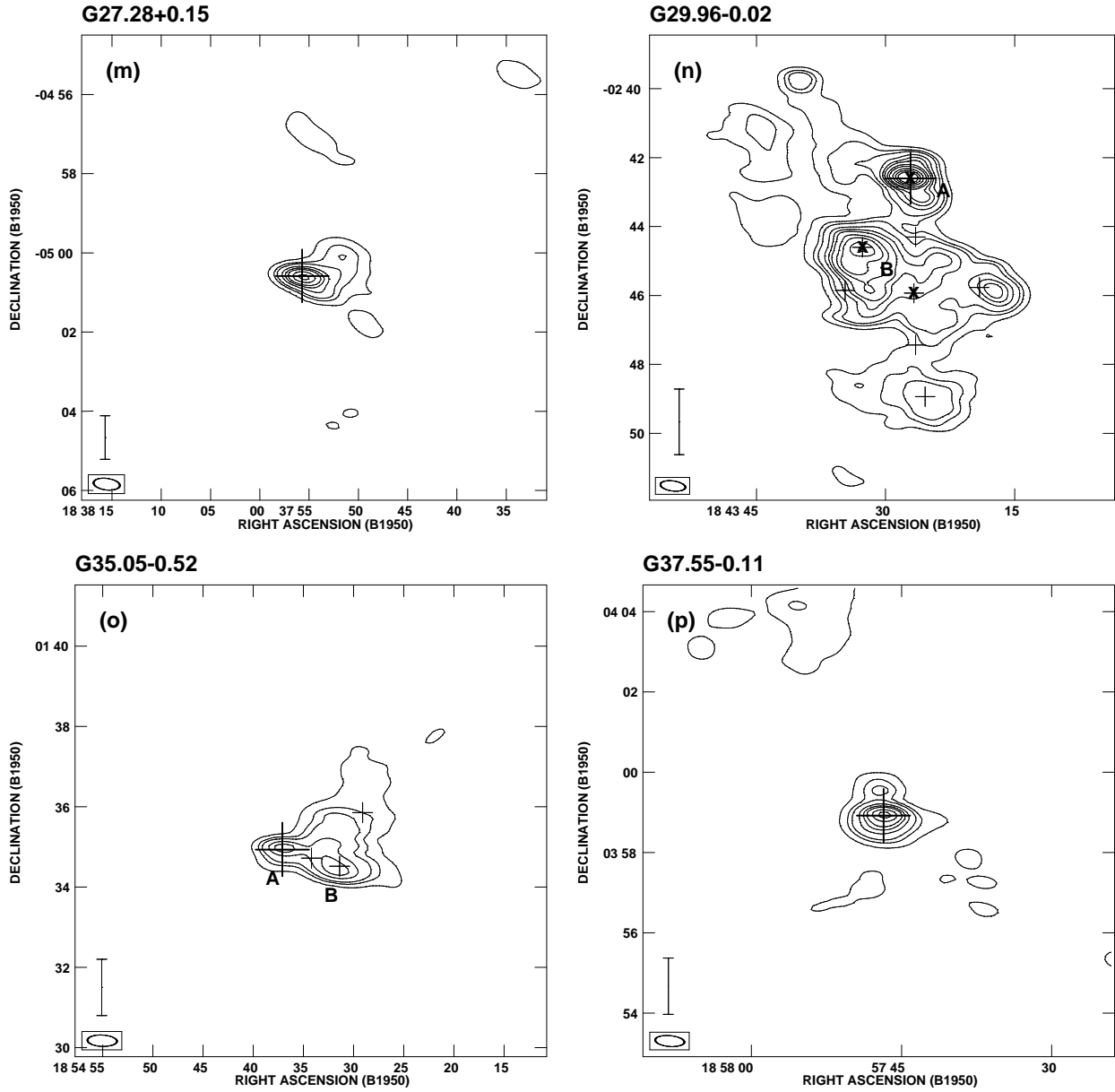


Fig. 1.— Radio continuum maps of 16 UC HII regions, made with the VLA (DnC array) at 21 cm. Contour levels are 10, 30, 50, 100, 150, 200, 300, 400, 600, 800, 1000, 1500, 2000, 2500, and 3000 mJy beam⁻¹. In each field, a large cross represents an UC HII region while small crosses are the positions where the H76 α line was observed. The “x” symbols mark the positions with detectable He76 α line emission (Table 6). In the sources with two or more compact components, A–C refer to the entries in Table 3. The synthesized beam and a 5 pc linear scale bar are shown in the bottom left corner. The linear scale assumes the distance given in Table 2.

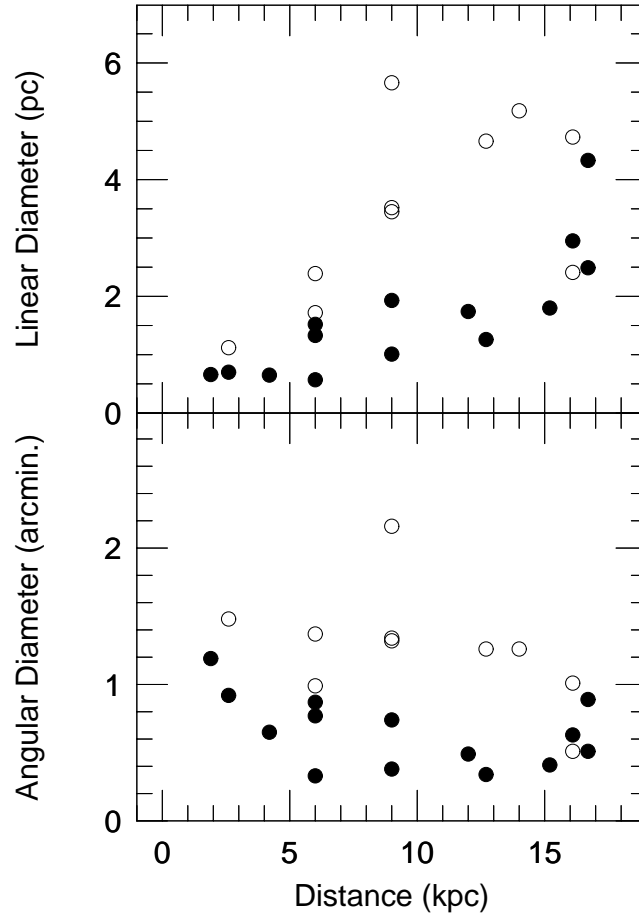


Fig. 2.— Plot of angular (*lower panel*) and linear (*upper panel*) sizes versus distance for the compact components. Filled and open circles represent the compact components with and without UC HII regions, respectively. The compact components with UC HII regions are generally smaller than those without UC HII regions.

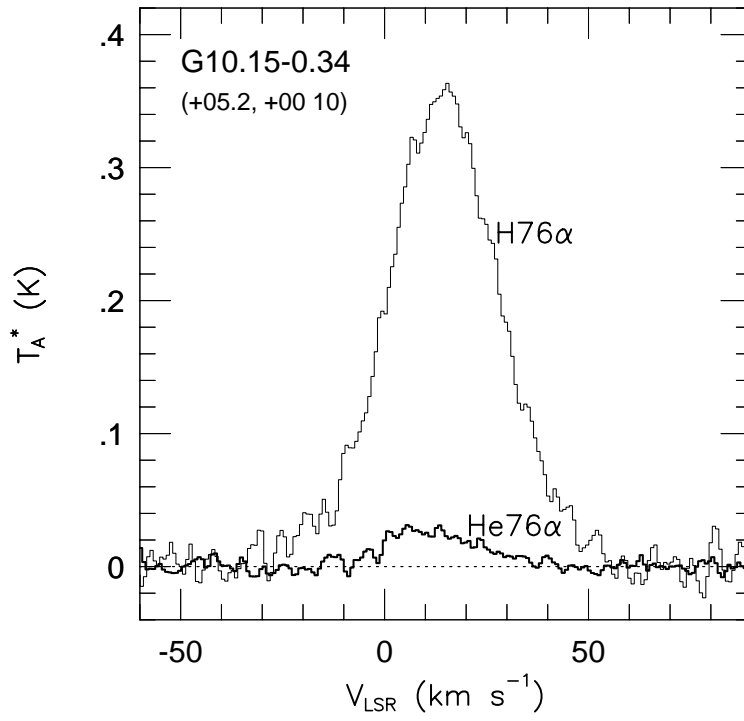


Fig. 3.— H76 α and He76 α radio recombination lines at G10.15–0.34 (+05 $^{\circ}$ 2, +00' 10 $''$), i.e., $(\alpha, \delta)_{1950} = (18^{\text{h}} 06^{\text{m}} 27^{\text{s}}.7, -20^{\circ} 19' 55'')$, where the strongest H76 α line emission was detected (Tables 5 & 6).

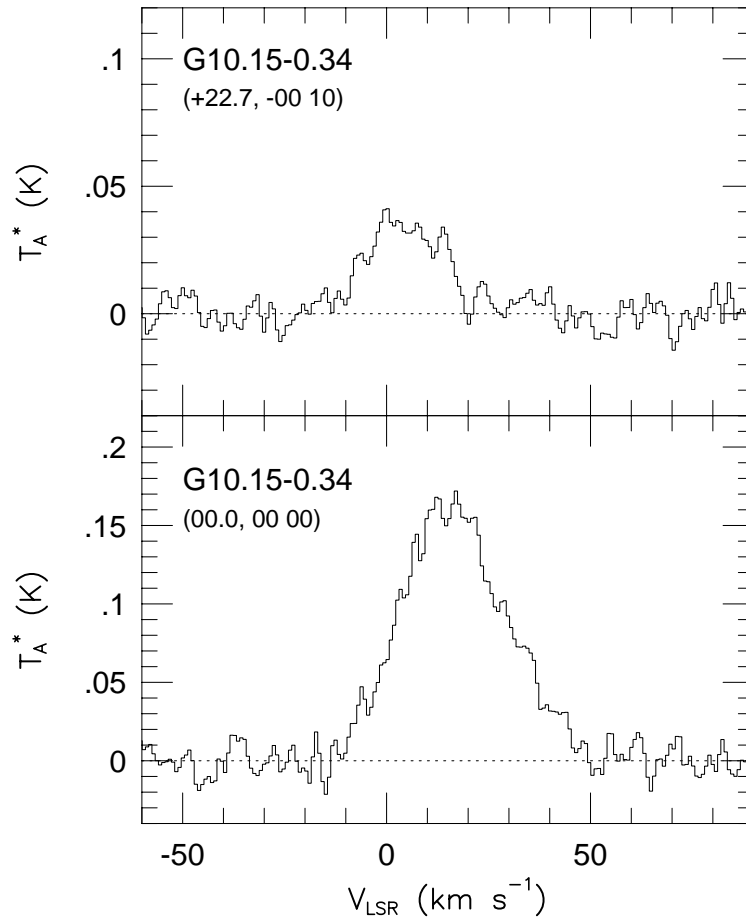


Fig. 4.— H76 α line profiles at G10.15–0.34 (+22 $^{\circ}$ 7, –00' 10'') and (00 $^{\circ}$ 0, 00' 00''). The former is blueshifted by about 10 km s $^{-1}$ with respect to the latter (Table 5). This suggests that the eastern protuberance may be a result of the champagne flow.

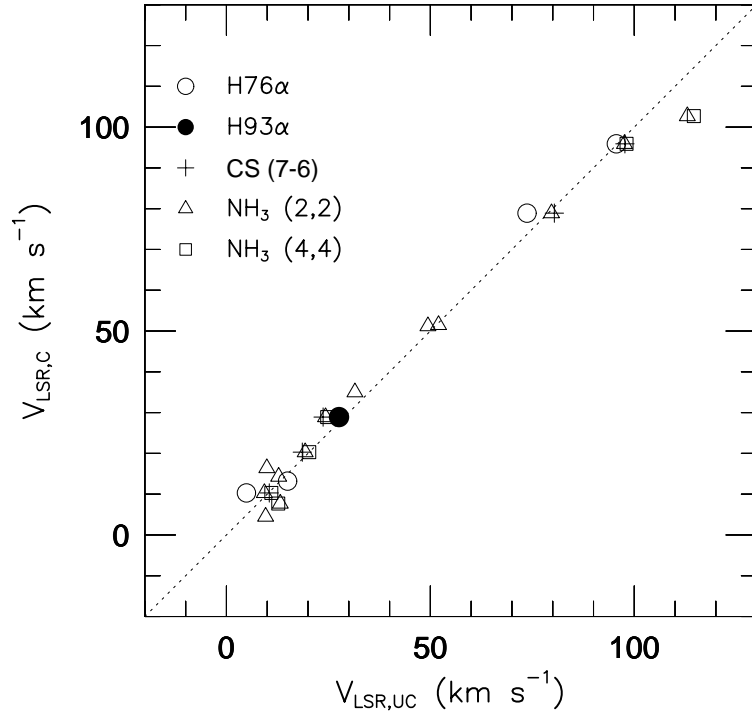


Fig. 5.— The central velocities of UC HII regions are compared with those of their associated compact components. H76 α , H93 α , CS (7–6), NH₃ (2,2), and NH₃ (4,4) lines are marked by open circles, filled circles, crosses, triangles, and squares, respectively. The dotted line represents $v_{\text{LSR,C}}=v_{\text{LSR,UC}}$.

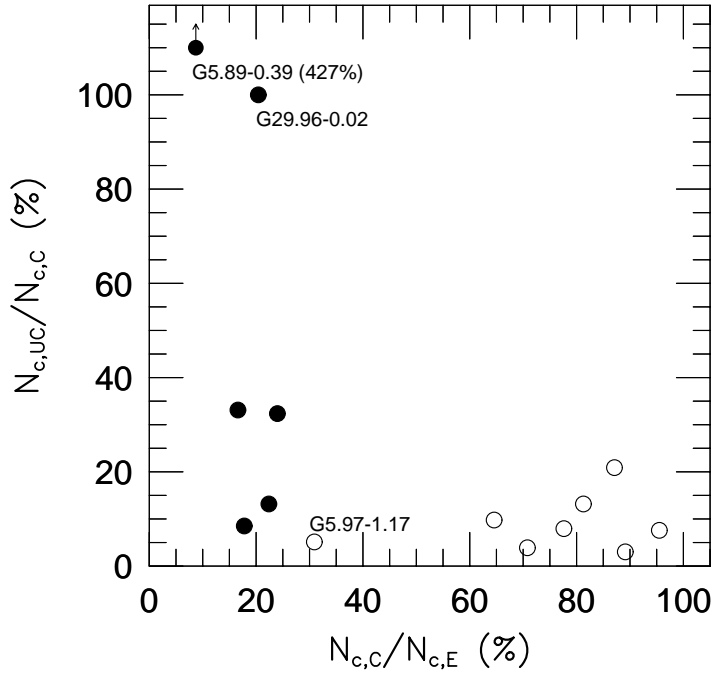


Fig. 6.— Comparison of $N'_{c,UC}/N'_{c,C}$ with $N'_{c,C}/N'_{c,E}$ for 14 sources in which UC HII regions have associated compact components. Here $N'_{c,UC}$, $N'_{c,C}$, and $N'_{c,E}$ are the Lyman continuum photon fluxes of the ultracompact, compact, and extended components, respectively. Open circles are sources with a single peak, while filled circles are sources with two or more compact components. For G5.89–0.39 and G29.96–0.02, $N'_{c,C}$ is equal to or less than $N'_{c,UC}$, probably due to a larger optical depth at 21 cm.

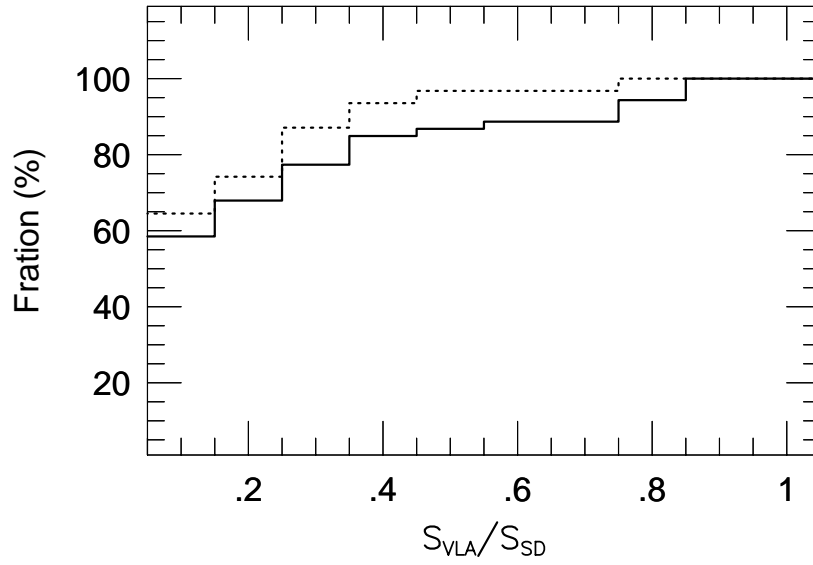


Fig. 7.— Variation of fraction (%) with ratio of VLA to single-dish fluxes, S_{VLA}/S_{SD} . The value at the ordinate is the number fraction of UC HII regions with smaller flux ratios than a given value at the abscissa. The solid line is drawn for 30 UC HII regions of simple morphology in the catalog of WC89, while the dotted line is for 22 simple UC HII regions in the catalog of KCW.

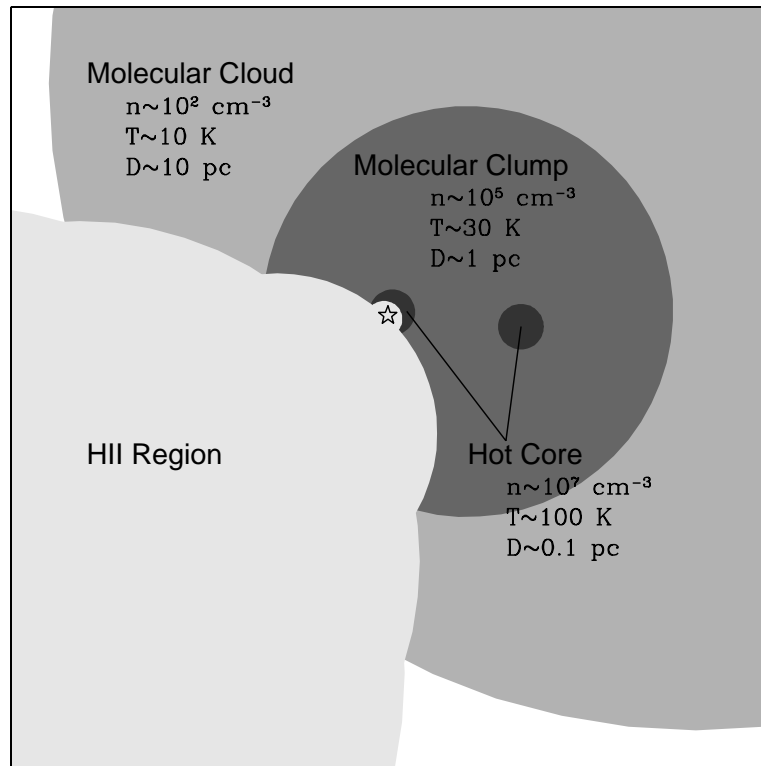


Fig. 8.— Schematic representation of our model that explains the origin of extended emission around an UC HII region using the Champagne flow model and the hierarchical structure of molecular clouds. An O star, marked by a star symbol, is located off-center within the hot core embedded in a molecular clump. The star maintains the ionization of the ultracompact, compact, and extended HII regions. This figure is not scaled. See the text for more details.

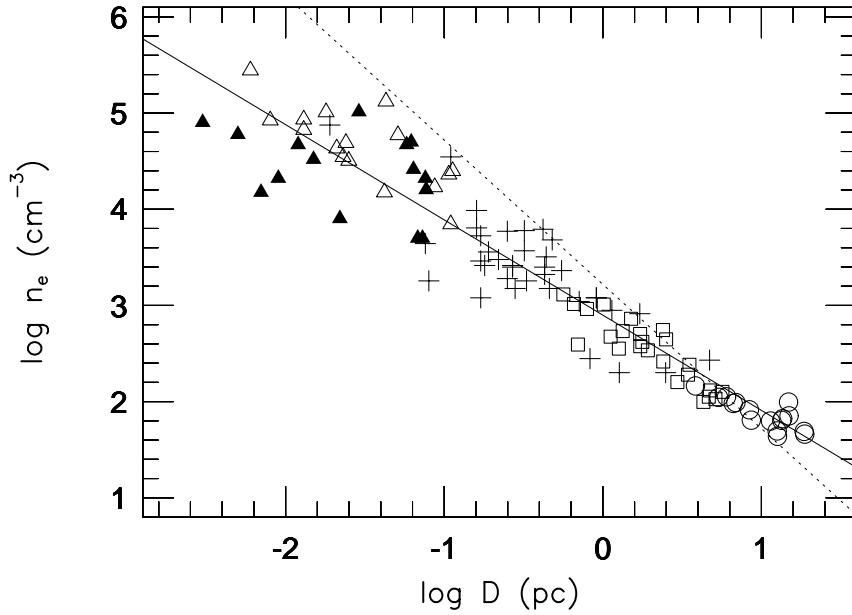


Fig. 9.— Plot of n_e against D . Various HII regions are marked: open triangles (*spherical UC ones in WC89*), filled triangles (*spherical UC ones in KCW*), crosses (*UC and compact ones in Garay et al. (1993)*), open squares (*compact ones in this work*), and open circles (*extended ones in this work*). A linear fit to all the data points gives $n_e=790 D^{-0.99}$ with a correlation coefficient of -0.95 . The solid and dotted lines represent the fitted relation and the line of a constant excitation parameter ($U=70$), respectively.

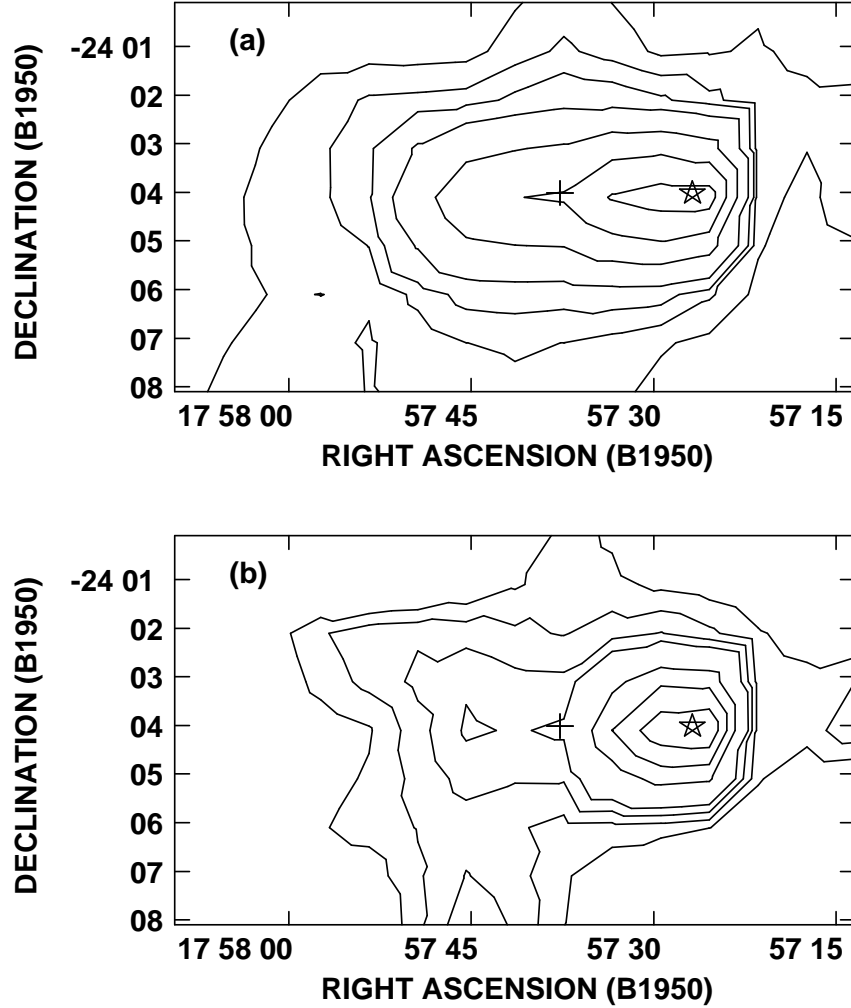


Fig. 10.— G5.89–0.39. (a) H76 α line integrated intensity map. Contour levels are 10, 15, 20, 30, 50, 70, and 90% of the peak value, 5.5 K km s⁻¹. Star and cross indicate the UC HII region and the central compact component, respectively. (b) H76 α equivalent line width ($\int T_L dv/T_L$) map. Contours correspond to 40, 45, 50, 55, 70, 80, and 90% of the peak value, 47.0 km s⁻¹.

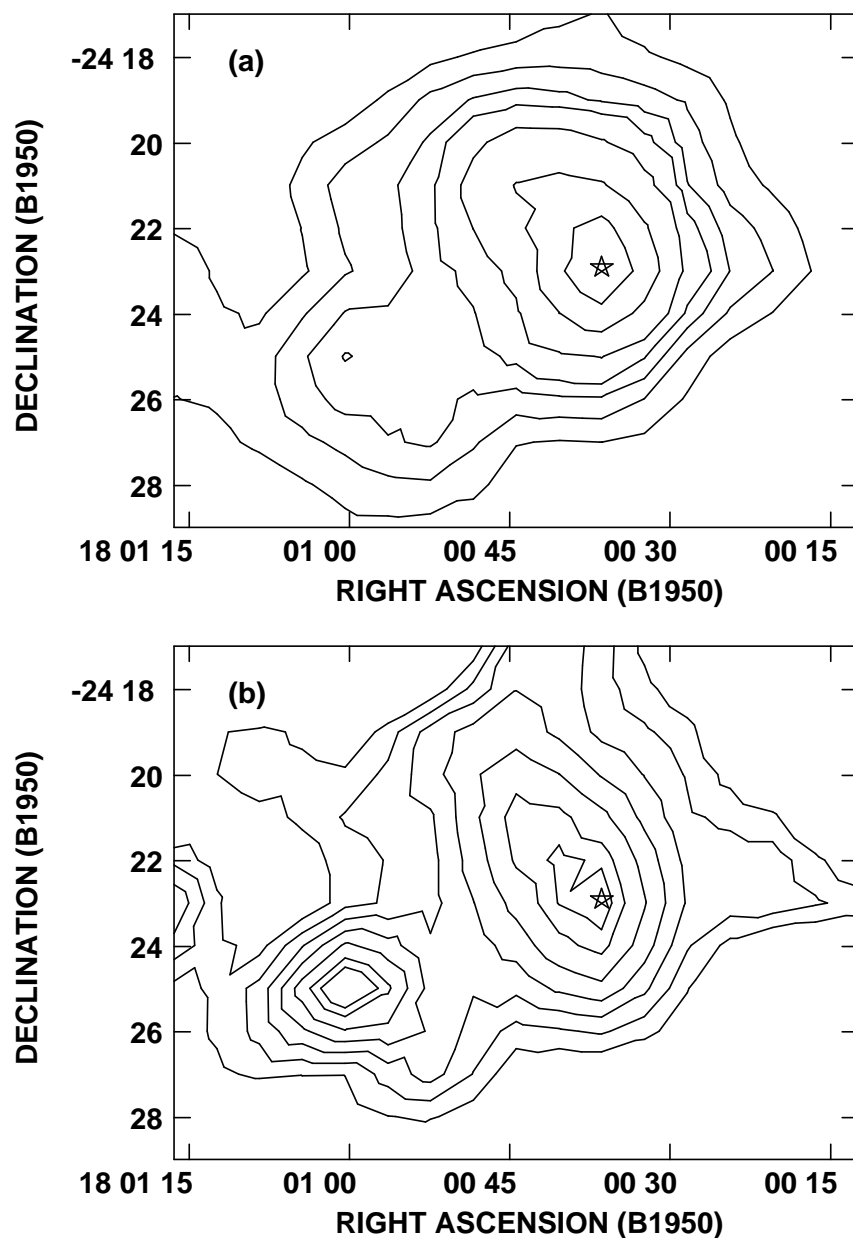


Fig. 11.— G5.97–1.17. (a) H76 α line integrated intensity map. Contours are 15, 20, 25, 30, 40, 60, and 80% of the peak value, 7.9 K km s⁻¹. Star marks the position of UC HII region. (b) H76 α equivalent line width ($\int T_L dv / T_L$) map. Contours correspond to 65, 70, 75, 80, 85, 90, and 93% of the peak value, 29.6 km s⁻¹.